Investigating time- and orientation-dependent transverse relaxation from magnetic susceptibility of white matter microstructure

Anders Dyhr Sandgaard¹, Rafael Neto Henriques², Noam Shemesh², Sune Nørhøj Jespersen^{1,3}

¹Center of Functionally Integrative Neuroscience, Department of Clinical Medicine, Aarhus University, Denmark

²Champalimaud Research, Champalimaud Centre for the Unknown, Lisbon, Portugal

³Department of Physics and Astronomy, Aarhus University, Denmark

Keywords

- 1) Magnetic susceptibility,
- 2) Transverse Relaxation,
 - 3) Diffusion,
 - 4) Microstructure
 - 5) Monte-Carlo

Corresponding Author: Anders Dyhr Sandgaard.

Mail: anders@cfin.au.dk

1 Abstract

Transverse relaxation in MRI is modulated by magnetic field variations arising from tissue microstructure, offering a potential window into the underlying chemical composition and structural organization at the cellular scale. However, the transverse relaxation rate in white matter depends on both echo time and the orientation of axons relative to the external field. Such anisotropy complicates the interpretation of transverse relaxation in general and as a biomarker for neurodegenerative disease. Understanding this anisotropy is therefore crucial for accurately analyzing MRI signals. While previous modeling studies have investigated these effects, they often relied on simplified or idealized tissue geometries. In this study, we investigate magnetic field variance and intra-axonal transverse relaxation using realistic axonal microstructure extracted from 3D electron microscopy, incorporating myelinated axons with embedded spherical susceptibility sources. We derive how transverse relaxation depends on

the angle between axons and the external magnetic field. Simulations show that the time-dependent power-law signature arising from white matter structural disorder is weak and may be difficult to detect at currently achievable noise levels, echo times, and field strengths. This is because the power-law curvature over a typical range of echo times deviates only slightly from a linear trend. Our findings highlight the influence of axonal geometry on intra-axonal transverse relaxation and suggest that accounting for both time and orientation dependence may facilitate the development of more precise neuroimaging biomarkers.

2 Introduction

Magnetic resonance imaging (MRI) is highly sensitive to water diffusion and microscopic magnetic field variations induced by tissue microstructure.

One way to probe these microscopic field variations is through their effect on the MR signal's relaxation. Transverse relaxation describes the loss of phase coherence among spins in the plane perpendicular to the main magnetic field B_0 in MRI, and results in decay of the signal over time. It is governed by several biophysical mechanisms, including molecular motion, tissue composition, and susceptibility-induced magnetic field inhomogeneities. Transverse relaxation, in particular, is sensitive to microscopic dephasing caused by magnetic field gradients generated by heterogeneous tissue environments such as myelinated axons^{1,2}, iron deposits^{3,4}, and blood vessels⁵⁻¹⁰. Myelinated axon bundles are predominantly found in white matter (WM), and they exhibit microscopic magnetic anisotropy due to both their orientational coherence and the tensorial susceptibility of myelin lipids¹¹⁻ ¹⁹. This anisotropy also leads to orientation-dependent phase shifts and transverse relaxation rates, meaning the MR signal varies with the subject's head orientation in the scanner. These effects complicate the interpretation of relaxation-based parameters and challenge their use as reliable biomarkers for neurodegenerative disease. In addition, other cellular components such as hemoglobinrich vasculature^{8,9,20-22}, iron-containing neuroglia²³, and mitochondria²⁴, as well as dipole-dipole interactions^{25,26}, are also likely to contribute to orientation-dependent relaxation due to their spatial organization in and around axons.

To better understand the origin of this orientation dependence, biophysical models have been developed to describe transverse relaxation analytically^{7,9,21,22,27–31}. These models often assume low volume fractions and idealized geometries, such as parallel hollow cylinders to mimic axons, or randomly oriented to model microvasculature, and spherical inclusions to mimic iron-rich cells. Recent frameworks have even extended the models to include multiple sources simultaneously, for example by modeling both myelin, vessels and iron inclusions as randomly distributed spheres^{32,33}.

However, oversimplified assumptions about geometry or diffusion can lead to predictions that do not match experimental observations. For example, idealized cylindrical models predict that transverse relaxation outside a cylinder varies as $\sin^4(\theta)$, with θ denoting the angle between the axon axis and the

external magnetic field B_0 , while no transverse relaxation is induced inside the cylinder. In contrast, Figure 1 illustrates how microscopic field perturbations generated by "synthetic axons" with different surface morphologies give rise to orientation-dependent Larmor frequency variance that differs from $\sin^4(\theta)$. For example, if the axon radius varies randomly both transverse and axially, a dipolar contribution, $(1 - \cos^2(\theta))^2$ can be found for intra-axonal Larmor frequency variance, which also adds to the orientation dependence of extra-axonal water such that its variance depends on a $\cdot \sin^4(\theta) + b \cdot (1 - \cos^2(\theta))^2$. When used as simplified representations of realistic axonal geometry, these examples show that realistic features - such as variations in cross-sectional area, axial undulations, and surface irregularities - produce orientation-dependent frequency variance and consequently orientation-dependent transverse signal decay. These effects cannot be captured by idealized, perfectly cylindrical geometries (Additional examples and quantitative details are provided in Supplementary Material S1).

Recent work³⁴ further demonstrates that more realistic WM morphologies generate magnetic field variations inside axons, leading to deviations from the $\sin^4(\theta)$ prediction. Moreover, experimental studies^{35–42} consistently suggest the presence of a dipolar contribution, $(1 - \cos^2(\theta))^2$, to transverse relaxation - an effect that cannot be explained by models based solely on ideal cylinders, orientation dispersion, or randomly positioned spheres. Although previous studies³⁶ have attributed this effect to myelin susceptibility anisotropy, this explanation remains unvalidated, as axially symmetric susceptibility aligned with cylindrical layers would not predict such observations¹⁸.

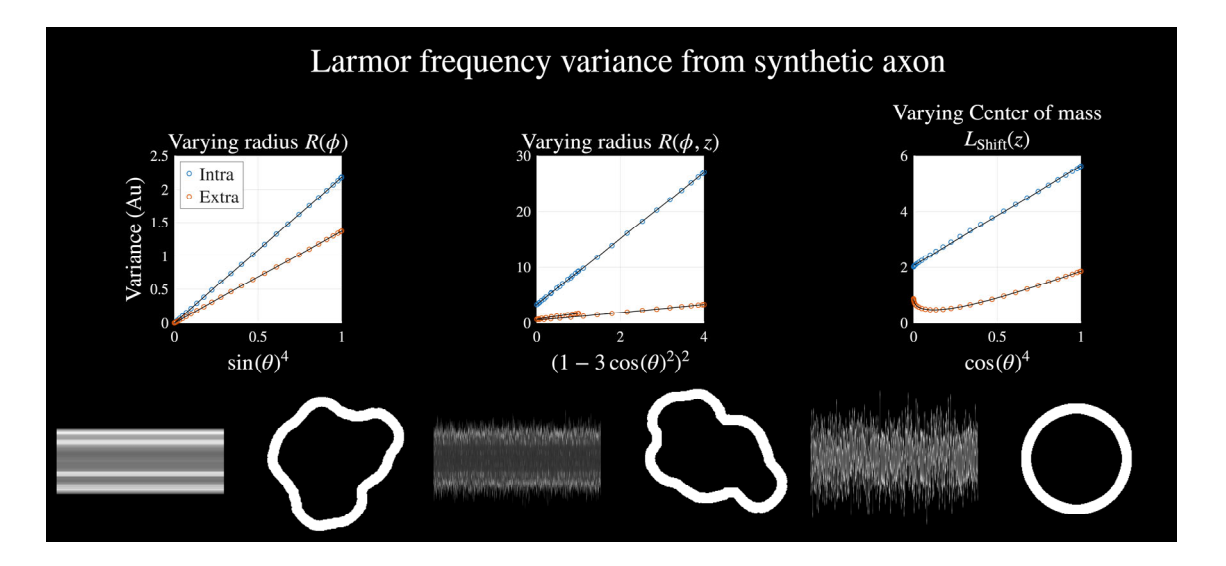


Figure 1 - Intra and extra-compartmental Larmor Frequency variance are shown for three different perturbations of a normal hollow cylinder. The left plot shows the variance if the radius varies randomly, but is fixed along the axis. In the middle plot, the tube radius varies randomly both transverse and axially. The right plot shows the Larmor frequency variance, where each axial slice

Not only the orientation, but also the time dependence of the signal relaxation depends in general on the structural disorder of the microstructure⁴³, where disorder here refers to deviations from regularity in the spatial arrangement of cellular components. Disorder is typically defined by a characteristic length scale, the correlation length l, which is the length beyond which correlations in spatial positions become negligible. This gives rise to an associated correlation time τ for spins diffusing with diffusivity D, corresponding to the time to diffuse past the correlation length $\tau \sim l^2/2D \sim 1-10$ ms, for most biological tissues⁴⁴. Ruh et al. derived⁴⁵ that the dimensionless, time-dependent transverse relaxation decay function $\eta(t)$, describing the normalized MR signal decay $\exp(-\eta(t))$, has a power law scaling $\eta(t) \sim (t/\tau)^{-v+2}$ if $v \neq 1$, and $\eta(t) \sim t/\tau \cdot \ln(t/\tau)$ if v = 1. This result applies when the signal decay is well approximated by the second signal cumulant and measured at times t longer than the microstructure's correlation time τ . Here v = (p + d)/2 is a dynamical exponent⁴³, where p defines the structural disorder class and d the effective dimensionality of the diffusion process, e.g., d = 3 for diffusion outside randomly positioned spheres or d=1 inside a long axon. For example⁴⁵, short-range (Poissonian) disorder describes systems in which a finite structural correlations length exist. A shortrange media has p = 0 and causes a time-dependent signal that decays as $\exp\left[-(t/\tau)^{\frac{4-d}{2}}\right]$. Hyperfluctuating disorder (p = -1), on the other hand, occurs in systems such as disordered arrays of long cylinders where the microstructure becomes increasingly correlated across longer distances⁴⁶. Such disordered media can lead to a time dependent signal $\exp\left[-(t/\tau)^{\frac{5-d}{2}}\right]$ for d=1,2 and $\exp\left[-\left(\frac{t}{\tau}\right)\cdot\ln\left((t/\tau)\right)\right]$ for d=3. It has been shown that intra-axonal space exhibit features of 1D short-range disorder due to variations in its axonal morphology⁴⁷, such as fluctuations in diameter and undulations along the axonal axis. These structural irregularities break the idealized cylinder models and thus influence the time dependence of transverse relaxation. However, each axon is also embedded within a dense and disordered environment of neighboring axons, cells and vasculature, and extracellular space, potentially introducing additional sources of short range or hyperfluctuating disorder from the extrinsic magnetic field perturbations they generate. This interplay between internal and external disorder complicates the relaxation dynamics and may give rise to signal decay behaviors that deviate from those predicted by simplified or isolated geometries.

Despite theoretical predictions and simulation-based studies, such time-dependent effects of transverse relaxation in realistic tissue microstructure remain largely unexplored. Moreover, it is still unclear whether these effects are detectable with practical MRI acquisition protocols. A deeper understanding of how microstructural disorder shapes relaxation dynamics is needed to determine whether such time dependencies can be meaningfully captured and interpreted in vivo.

It is also well known that WM microstructure contains orientationally dispersed axonal bundles. In highly anisotropic regions such as the corpus callosum (CC), axons typically exhibit around 20 degrees of dispersion^{48,49}, whereas other WM regions contain multiple crossing fiber bundles. As a result, the MRI signal must account not only for different water compartments inside and outside of axons, but also for axonal bundles with varying orientations. In diffusion MRI, the WM signal is generally modeled as originating from multiple non-exchanging mesoscopic axonal bundles with directions \hat{n} . Mesoscopic refers here to the scale ($\sim 100 \,\mu m$) that is larger than the typical cell size ($\sim 1-10 \,\mu m$) but smaller than the imaging resolution (~1 mm). The signal from a single bundle is described by a mesoscopic signal kernel $\mathcal{K}(b, \hat{\boldsymbol{n}} \cdot \hat{\boldsymbol{g}})$ where $b, \hat{\boldsymbol{g}}$ represents the diffusion weighting 50. This kernel accounts for both intraaxonal and extra-axonal Gaussian signals, which is a valid assumption for long diffusion times compared to the time to diffuse across the characteristic length scale l of the microstructure. The total signal from a collection of axonal bundles with various orientations is then modeled as a convolution over directions $\hat{\mathbf{n}}$, $S(b, \hat{\mathbf{g}}) = \mathcal{K}(b, \hat{\mathbf{n}} \cdot \hat{\mathbf{g}}) \otimes \mathcal{P}(\hat{\mathbf{n}})$, where $\mathcal{P}(\hat{\mathbf{n}})$ is the fiber orientation distribution function (fODF)⁵⁰. This framework, with axons further approximated as sticks, is known as the Standard Model of Diffusion in White Matter^{50,51}, and extensions incorporating compartmental isotropic transverse relaxation have been proposed^{38,52,53}. A similar concept has also been proposed to describe the multi-gradient-echo (MGE) signal from orientationally dispersed bundles with orientationdependent Larmor frequency shifts⁵⁴. However, none of these models incorporating orientation dispersion have accounted for orientation-dependent transverse relaxation effects caused by the morphology of individual axons.

The aim of this study is to identify which specific microstructural features are most influential in shaping transverse relaxation, thereby guiding future modeling efforts based on realistic WM architecture. To do so, we investigate the functional dependence of transverse relaxation on both time and orientation, as a means to probe the magnetic microstructure of white matter (WM). Using a newly developed Monte Carlo (MC) simulation framework, we model the mesoscopic MR signal for both multi-gradient-echo (MGE) and asymmetric spin-echo (ASE) sequences in mesoscopically sized WM segments containing coherently oriented axons and randomly positioned intra-axonal spheres.

First, we examine the time dependence of transverse relaxation in WM to see if it exhibits features consistent with short-range or hyperfluctuating structural disorder. Second, we investigate how the simulated signals depend on the underlying magnetic field perturbations generated by realistic microstructure, comprising uniformly magnetized, myelinated axons and spherical inclusions, by comparing transverse relaxation to the corresponding magnetic field variance.

Additionally, we derive how transverse relaxation in an axially symmetric microstructure varies with the orientation of the axonal bundle relative to the main field B_0 , and compare this prediction to

simulation results. We also assess whether realistic microstructure alone can account for experimentally observed orientation-dependent transverse relaxation without invoking anisotropic susceptibility.

3 Theory MR signal

We consider a magnetized random medium within a mesoscopic volume \mathcal{M} , containing non-exchanging water compartments. The magnetized medium, described by a scalar magnetic susceptibility $\chi(\mathbf{r})$, induces a microscopically varying magnetic field

$$\Delta \mathbf{B}(\mathbf{r}) \simeq \int_{\mathcal{M}} d\mathbf{r}' \, \mathbf{Y}(\mathbf{r} - \mathbf{r}') \chi(\mathbf{r}') \widehat{\mathbf{B}}. \tag{1}$$

Here $\mathbf{Y}(\mathbf{r})$ is the dipole field tensor and $\mathbf{B}_0 = B_0 \mathbf{\hat{B}}$ is the external field. The induced field gives rise to a microscopically varying Larmor frequency distribution $\Omega(\mathbf{r}) \simeq \gamma B_0 \mathbf{B}^T \Delta \mathbf{B}(\mathbf{r})$. We denote the *intra-compartmental* field mean, variance and standard deviation as Ω_c , σ_c^2 and σ_c respectively, for each compartment labeled by c.

Since the signal decay is generally not mono exponential, there is not a single, well-defined relaxation rate. For generality, we therefore write the total MRI signal for a Free-Induction-Decay (FID) as a normalized exponentially decaying function $S(t) = \exp(-\eta_{FID}(t) - i\varphi_{FID}(t))$, where $\eta_{FID}(t)$ describes the dimensionless time-dependent accumulated transverse relaxation of the total signal across all water compartments, and $\varphi_{FID}(t)$ the net accumulated phase at time t. At each time point, we can define an accumulated relaxation rate as $R_2 = \eta_{FID}/t$. We henceforth omit \mathbf{B}_0 and t for notational simplicity.

For the signal in a compartment c, we write $S_c = \exp(-\eta_c - i\varphi_c)$. Assuming the signal's characteristic phase variance is sufficiently small⁵⁵ such that $\sigma_c \tau \ll 1$, the compartmental signal frequency and relaxation can be described by the first and second signal cumulants $\varphi_c = \langle \varphi \rangle = t\Omega_c$, $\eta_c = \langle \varphi^2 \rangle / 2$, respectively. The phase of a spin is $\varphi = \int_0^t dt' \, \Omega(\mathbf{r}_{t'})$ and describes the accumulated phase shift along its stochastic trajectory $\mathbf{r}(t')$. The brackets $\langle ... \rangle$ relate to the average over spins. If the characteristic phase is stronger, φ_c , η_c may depend on higher order cumulants. The first and second cumulant relate to the spatially varying Larmor frequency distribution and variance Ω_c and σ_c^2 , inside the axon. Notice that the first cumulant, describing the signal phase, depends directly on the average induced magnetic field $\overline{\Delta B}$, cf. Eq. (1), while the second cumulant can also be affected by diffusion. When the decay is weak, $\eta_c \ll 1$, and the effect of diffusion is negligible, i.e. $t \ll \tau$, the signal decay becomes $\eta_c(t) \simeq \sigma_c^2 t^2/2$. When $t \gg \tau$, as described in the introduction, the functional form of the time dependence t0. Notice that if the field

variance exhibits hyperfluctuating disorder within 1D diffusing water compartments (v = 0), which may originate from magnetic field variance in the intra-axonal space, induced by other axons, the two regimes, $t \gg \tau$ and $t \ll \tau$, have identical time dependence.

In the next sections, we show how the signal decay depends on the varying Larmor frequency distributions, when the medium consists of multiple signal-generating compartments.

MR signal - Multiple water compartments

Consider a medium consisting of multiple water compartments, labeled by c. These could be all the axons in a coherent bundle. Here the net normalized FID signal can be written as

$$S = \exp(-\eta^{FID} - i\varphi^{FID}) = \sum_{c} f_c S_c = \sum_{c} f_c \exp(-\eta_c - i\varphi_c), \tag{2}$$

where $\sum_{c} f_{c} = 1$ defines the signal fractions.

When compartmental signals differ only weakly from a characteristic decay, the dominant effects can be captured by a Taylor expansion. In diffusion MRI, this is formalized through the cumulant expansion used in DTI and DKI, which expands $\ln(S)$ in powers of $b\overline{D}$. Here b refers to the diffusion weighting strength and \overline{D} the average diffusivity. Expanding the logarithm yields cumulants, quantities that are better conditioned, more robust to noise, and often provide accurate approximations with fewer terms than moment expansions. We apply the same principle here. If compartmental morphologies vary slightly, the total free-induction decay η^{FID} depends not only on the mean decay η_c and phase φ_c but also on their inter-compartmental variances. This follows from a second-order expansion of $\ln(S)$ (cf. Eq. (2)) around the compartment-weighted averages $\overline{\eta} = \sum_c f_c \eta_c$ and phase shift $\overline{\varphi} = \sum_c f_c \varphi_c$, where $\overline{(\dots)} = \sum_c f_c(\dots)_c$ denotes the mean over compartments (intercompartmental mean). Notice that $\overline{\eta} + i\overline{\varphi}$ is analogous to $b\overline{D}$ in our case. For convenience, we define $\overline{\varphi^2} - \overline{\varphi}^2 = \sum_c f_c (\varphi_c - \overline{\varphi})^2$ as the intercompartmental variance of intra-compartmental mean phase shifts, $\overline{\eta^2} - \overline{\eta}^2 = \sum_c f_c (\eta_c - \overline{\eta})^2$ as the intercompartmental variance of intra-compartmental signal decay functions, and lastly the intercompartmental covariances as $\overline{\eta}\overline{\varphi} - \overline{\eta} \cdot \overline{\varphi} = \sum_c (\eta_c - \overline{\eta})(\varphi_c - \overline{\varphi})$.

Rewriting the logarithm of the signal with respect to $\overline{\eta} + i \overline{\varphi_c}$ we get

$$\ln(S) = \log \left(\exp(-\overline{\eta} - i\overline{\varphi}) \sum_{c} f_{c} \exp(-(\eta_{c} - \overline{\eta}) - i(\varphi_{c} - \overline{\varphi})) \right).$$

Using the logarithmic rules $\ln(\exp(A) \cdot B) = A + \ln(B)$, along with the Taylor expansions $\ln(x) \approx -1 + x$ (for $x \to 1$) and $\exp(-x) \approx 1 - x + x^2/2$ (for $x \to 0$), the logarithm of the signal becomes

$$\ln(S) \approx \left((-\overline{\eta} - i\overline{\varphi}) - 1 + \sum_{c} f_{c} \left(1 - (\eta_{c} - \overline{\eta}) - i(\varphi_{c} - \overline{\varphi}) + \frac{1}{2} \left((\eta_{c} - \overline{\eta}) + i(\varphi_{c} - \overline{\varphi}) \right)^{2} \right) \right).$$

As $\sum_c f_c = 1$, it cancels out the -1. Second, the sums $\sum_c f_c(\eta_c - \overline{\eta}) = \overline{\eta} - \overline{\eta} = 0$, and $\sum_c f_c(\varphi_c - \overline{\varphi}) = 0$. Writing out the second order term explicitly, we arrive at the four main contributions

$$= \left((-\overline{\eta} - i\overline{\varphi}) - \frac{1}{2} \sum_{c} f_{c} (\varphi_{c} - \overline{\varphi})^{2} + \frac{1}{2} \sum_{c} f_{c} (\eta_{c} - \overline{\eta})^{2} + i \sum_{c} f_{c} (\eta_{c} - \overline{\eta}) (\varphi_{c} - \overline{\varphi}) \right).$$

Taking the exponential on each side, we thus get

$$S = \exp\left(-\overline{\eta} - i\overline{\varphi} - \frac{1}{2}(\overline{\varphi^2} - \overline{\varphi}^2) + \frac{1}{2}(\overline{\eta^2} - \overline{\eta}^2) + i(\overline{\eta}\overline{\varphi} - \overline{\varphi} \cdot \overline{\eta})\right). \tag{3}$$

Assuming the compartmental signal phase $\varphi_c = \Omega_c t$ is described by the spatially averaged Larmor frequency shift Ω_c , cf. Eq. (1), we can rewrite the phase contribution in terms of the Larmor frequency shift $\overline{\varphi} = t\overline{\Omega}$ and $\overline{\varphi^2} - \varphi^2 = t^2\left(\overline{\Omega^2} - \overline{\Omega}^2\right)$. This means that intercompartmental Larmor frequency variance $\overline{\varphi^2} - \overline{\varphi}^2$ gives rise to a signal exponentially decaying with t^2 , while variance $\overline{\eta^2} - \overline{\eta}^2$ in the compartmental signal decay functions $\eta_c(t)$ reduces the overall signal decay rate in a manner analogous to the effect of kurtosis⁵⁶ in DKI. The net FID signal decay η_{FID} thus becomes

$$\eta^{FID}(t) = \overline{\eta}(t) + \frac{1}{2} \left(\overline{\varphi^2} - \overline{\varphi}^2 \right) - \frac{1}{2} \left(\overline{\eta^2}(t) - \overline{\eta}(t)^2 \right) \tag{4}$$
(FID signal decay)

Notice $\overline{\eta} \propto (\gamma B_0 \chi)^2$, $\overline{\eta^2} - \overline{\eta}^2 \propto (\gamma B_0 \chi)^4$ and $\overline{\varphi^2} - \overline{\varphi}^2 \propto (\gamma B_0 \chi)^2$ when the individual compartmental signal decays are described by the second cumulant with respect to the scaling parameters $\gamma B_0 \chi$. For a spin-echo (SE) signal, the inter-compartmental phase variance will be refocused, and the decay $\eta^{SE}(t)$ becomes

$$\eta^{SE}(t) = \overline{\eta}(t) - \frac{1}{2} \left(\overline{\eta^2}(t) - \overline{\eta}(t)^2 \right). \tag{5}$$

(SE signal decay)

We emphasize that the mean decay $\overline{\eta}$ is different between FID and SE, and should be smaller for SE compared to FID, since the intra-compartmental decay η_c are partly refocused by the 180-degree RF pulse.

To re-iterate: each intra-compartment signal S_c may be described by a cumulant expansion of the signal up to second order if $\sigma_c \tau \ll 1$. Then, the sum *across* compartments can *also* be written as a cumulant expansion, if the compartmental decay functions η_c do not vary too much across compartments. Here the variance $\overline{\eta^2} - \overline{\eta}^2$ scales as fourth order in B_0 , and therefore appears in the fourth order cumulant of the net signal S. Since $\sigma_c \tau \ll 1$ per definition, we thus expect $\overline{\eta^2} - \overline{\eta}^2$ to have a negligible impact on the net decay function η , but we keep it for now. For long echo times $t \gg \tau$ compared to the correlation time τ , these different terms of Eqs. (4) and (5) scale with time as $\overline{\eta} \propto t^{-2\nu+2}$, $\overline{\eta^2} - \overline{\eta}^2 \propto t^{-4\nu+4}$ and $\overline{\varphi^2} - \overline{\varphi}^2 \propto t^2$, while for short times where $t \ll \tau$, $\overline{\eta} \propto t^2$, $\overline{\eta^2} - \overline{\eta}^2 \propto t^4$ and $\overline{\varphi^2} - \overline{\varphi}^2 \propto t^2$. Hence, three potential contributions from the internal field with unique time dependences may contribute to the signal's relaxation.

As the induced Larmor frequency shift depends on orientation, so does $\overline{\eta}$, $\overline{\eta^2} - \overline{\eta}^2$ and $\overline{\varphi^2} - \overline{\varphi}^2$. We therefore consider the orientation dependence of the net signal decay in the next section.

Orientation dependence of second signal cumulant

Here we show that, for weakly magnetized tissue with axially symmetric microstructure, the orientation dependence of the transverse relaxation decay includes only even-order cosines up to fourth order. As described above, the transverse relaxation is fully defined by the second cumulant $\eta = \langle \varphi^2 \rangle / 2$, caused by the microstructure's induced magnetic field. The second cumulant of a signal from a sequence described by a general spin flip function $\xi(t)$ (for example a 180-degree RF pulse for a spin echo sequence) is

$$\langle \varphi^{2} \rangle = \int_{0}^{t} dt \int_{0}^{t} dt' \, \xi(t) \xi(t') \langle \Omega(\mathbf{r}_{t}) \Omega(\mathbf{r}_{t'}) \rangle , \qquad (6)$$

$$\simeq (\gamma B_{0})^{2} \int_{0}^{t} dt \int_{0}^{t} dt' \, \xi(t) \xi(t') \int_{\mathcal{M}} d\mathbf{r} \int_{\mathcal{M}} d\mathbf{r}' \, \widehat{\mathbf{B}}^{\mathsf{T}} \mathbf{Y}(\mathbf{r}) \widehat{\mathbf{B}} \widehat{\mathbf{B}}^{\mathsf{T}} \mathbf{Y}(\mathbf{r}') \widehat{\mathbf{B}} \langle v^{w}(\mathbf{r}_{t}) v(\mathbf{r}_{t} + \mathbf{r}) v^{w}(\mathbf{r}_{t'}) v(\mathbf{r}_{t'} + \mathbf{r}') \rangle .$$

Here we made a change of variables such that the dipole kernel does not depend on the time-dependent particle position. We now write out the dipole fields to yield

$$\widehat{\mathbf{B}}^{\mathsf{T}}\mathbf{Y}(\boldsymbol{r})\widehat{\mathbf{B}}\widehat{\mathbf{B}}^{\mathsf{T}}\mathbf{Y}(\boldsymbol{r}')\widehat{\mathbf{B}} \propto \frac{1}{r^3} \frac{1}{{r'}^3} \Big(1 - 3\big(\widehat{\boldsymbol{r}} \cdot \widehat{\mathbf{B}}\big)^2\Big) \Big(1 - 3\big(\widehat{\boldsymbol{r}}' \cdot \widehat{\mathbf{B}}\big)^2\Big).$$

For simplicity and without loss of generality in axially symmetric microstructure, we choose the symmetry axis to be \hat{z} and take $\hat{\mathbf{B}} = [\sin(\theta) \ 0 \cos(\theta)]^T$, so the angular part can be rewritten as

$$(1 - 3(\hat{r} \cdot \hat{\mathbf{B}})^{2})(1 - 3(\hat{r}' \cdot \hat{\mathbf{B}})^{2})$$

$$= 1$$

$$- 3((\hat{r}_{x}'^{2} + \hat{r}_{x}^{2})\sin^{2}(\theta) - (\hat{r}_{z}'^{2} + \hat{r}_{z}^{2})\cos^{2}(\theta)$$

$$- 2(\hat{r}_{x}'\hat{r}_{z}' + \hat{r}_{x}\hat{r}_{z})\sin(\theta)\cos(\theta))$$

$$+ 9(\hat{r}_{x}'^{2}\hat{r}_{x}^{2}\sin^{4}(\theta) + \hat{r}_{z}'^{2}\hat{r}_{z}^{2}\cos^{4}(\theta)$$

$$+ 4(\hat{r}_{x}'^{2}\hat{r}_{z}^{2} + \hat{r}_{x}^{2}\hat{r}_{z}'^{2} + \hat{r}_{x}'\hat{r}_{z}'\hat{r}_{x}'\hat{r}_{z}')\cos^{2}(\theta)\sin^{2}(\theta)$$

$$+ 2(\hat{r}_{z}'^{2}\hat{r}_{x}\hat{r}_{z} + \hat{r}_{z}^{2}\hat{r}_{x}'\hat{r}_{z}')\cos(\theta)\sin^{3}(\theta)$$

$$+ 2(\hat{r}_{z}'^{2}\hat{r}_{x}\hat{r}_{z} + \hat{r}_{z}^{2}\hat{r}_{x}'\hat{r}_{z}')\cos^{3}(\theta)\sin(\theta)).$$
(7)

Consider the terms above with odd order combinations of sines and cosines. For axially symmetric microstructure, the second cumulant must satisfy antipodal symmetry, meaning that it remains unchanged under the transformation $\theta \to \pi - \theta$. All odd angular terms violate this symmetry and therefore cannot contribute. Consequently, the orientation dependence is fully determined by even-order cosine terms only.

$$\eta = a \cdot \cos^4(\theta) - b \cdot \cos^2(\theta) + c. \tag{8}$$

This result is valid for a general pulse sequence and should thus describe both η^{FID} and η^{SE} . As the result is independent of diffusion dynamics and spin flip function $\xi(t)$, the functional form is also valid for the magnetic field variance (this is demonstrated in Supplementary material S2).

The amplitudes, except a, may be negative as long as η is positive overall for all θ . For example, the variance outside a straight cylinder scales as $\sin^4(\theta) = 1 - 2\cos^2(\theta) + \cos^4(\theta)$. A similar orientation dependence occurs inside and outside a long tube whose cross-section varies randomly but does not change along its axis. The variance outside anisotropically positioned spheres (an analogy could be a string of beads⁵⁷) scales as $(1 - 3\cos^2(\theta))^2 = 1 - 6\cos^2(\theta) + 9\cos^4(\theta)$. Hence, different structural features leads to different weights a, b, c, and each may in general reflect combined effects of multiple features. Notice all the exemplified structures mentioned here produced a negative amplitude b. To second order of the cumulant expansion, this result therefore holds for both the net signal decay and the magnetic field variance σ^2 , and both are investigated here with simulations. While such orientation dependence of Eq. (8) has been proposed before, e.g. by imposing susceptibility anisotropy³⁶ or dipole-dipole interactions with the myelin sheath²⁶, the novelty here is that we arrived at it assuming only an axially symmetric and translation invariant microstructure with uniform (scalar) susceptibility.

Relating the total signal decay function to a second order cumulant expansion across water compartments with different decay functions η_c is justified only when the variability in η_c and Ω_c across compartments is sufficiently small. However, in a macroscopic voxel, e.g. in WM, there exist multiple bundles of axons oriented differently to the external $\mathbf{B_0}$ field, which can challenge the validity of this compartmental expansion. Second, water in the extra-axonal space in WM may also experience a different total decay function η_e , which requires separation of intra- and extra-axonal space on the mesoscopic scale. Hence, if we consider a macroscopic volume consisting of multiple mesoscopic subvolumes \mathcal{M} , where the mesoscopic signal $\mathcal{K}_{\mathcal{M}}$ is well approximated by the second order expansion across its compartments, e.g. coherent bundles of axons with different orientations $\hat{\mathbf{n}}$, the net signal becomes a sum

$$S = \sum_{\mathcal{M}} \mathcal{K}_{\mathcal{M}} = \sum_{\mathcal{M}} \exp(-\eta_{\mathcal{M}} - i\varphi_{\mathcal{M}}).$$

(9)

(multiple mesoscopic regions)

Here the notation $\mathcal{K}_{\mathcal{M}}$ is motivated by the Standard Model of diffusion (SM) in WM⁵⁰. Applying this to WM, we consider the axonal microstructure as a random medium consisting of many orientationally dispersed bundles of aligned axons. We categorize the MR fluids as intra-axonal (a) and extra-axonal water (e), where every axon bundle is assumed to be described by the same signal kernel (myelin water is assumed to be fully relaxed). As axonal bundles can have different orientations \hat{n} , we replace the sum over \mathcal{M} with an integration over a fiber orientation distribution function $\mathcal{P}(\hat{n})$,

$$S = S_0 \int d\widehat{\boldsymbol{n}} \, \mathcal{P}(\widehat{\boldsymbol{n}}) \mathcal{K}(\widehat{\boldsymbol{n}}), \tag{10}$$

where

$$\mathcal{K}(\widehat{\boldsymbol{n}}) = f_a \exp(-\eta_a(\widehat{\boldsymbol{n}}) - i\varphi_a(\widehat{\boldsymbol{n}}))$$

$$+ (1 - f_a) \exp(-\eta_e(\widehat{\boldsymbol{n}}) - i\varphi_e(\widehat{\boldsymbol{n}}))$$
(11)

(WM signal)

is the mesoscopic signal kernel and depends on the angle between the axons and external field. The decay functions η_a and η_e is described by Eqs. (4) and (8), but η_e has no contribution from intercompartmental variance, since the extra-axonal space only consists of one water compartment, and hence all variance is intra-compartmental per definition. As we assume each bundle is characterized by the same signal kernel \mathcal{K} , the transverse relaxation rate in each bundle originates *statistically* from similar local microstructure, only oriented differently with respect to the external field. The transverse relaxation induced between neighboring bundles is also orientation dependent, but contributes equally to each bundle, as the microstructure external to each bundle should look the same assuming a

translation invariant random medium. Transverse relaxation from other field variations also affects the signal - both on the molecular scale (e.g., dipole-dipole relaxation^{25,26}) and macroscopic scale (e.g., macroscopic variations across the extent of the point-spread-function⁵⁸), but these are not considered in this study.

4 Methods

All simulations and analyses were done in Matlab (The MathWorks, Natick, MA, USA). All animal experiments were preapproved by the competent institutional and national authorities and carried out according to European Directive 2010/63.

Supplementary material contains additional simulations where we computed the Larmor frequency variance from both the realistic and synthetically generated axons created by perturbing the surface of an ideal cylinder. Those simulations allowed us to validate our simulation framework and to investigate how different microstructural features impacted the orientation dependence. Investigating the induced field variance from both individual axons and the whole microstructure also enabled us to assess the importance of magnetic field variances induced from neighboring axons and from different types of magnetic inclusions.

Simulations: Investigating transverse relaxation inside realistic axonal microstructure

We designed a set of simulations to examine the orientation dependence of Eqs. (4) and (8) from full WM axonal microstructures from EM containing thousands of axons. We considered the individual contribution from magnetic fields induced i) by the axons and ii) manually introduced intra-axonal spherical inclusions. Every inclusion, also myelin, was assumed to have scalar susceptibility^{11,59} in every simulation. For each substrate, we identified the principal fiber direction and selected a major axon bundle consisting of approximately 2,000 axons aligned predominantly along this direction. As described in our previous study¹², the axonal microstructure in each substrate was defined by an indicator function v(r) on a 3D grid with resolution of 0.1 μ m³ (see ref ¹² for more details).

For the myelinated axons in *i*), we used an intrinsic scalar susceptibility of $\chi_{\rm m}=-100\frac{\rm ppb}{\zeta_{\rm m}}^{11,59,60}$, where ζ_m is the volume fraction of axons in the entire microstructure. The local Larmor frequency shift $\Omega(r)$ was calculated numerically⁶¹ using Eq. (1), with $\chi_m(r)=\chi_m v_m(r)$ for 50 unique orientations of $\widehat{\bf B}$ generated using electrostatic repulsion⁶². As our simulation resolution (0.1 μ m³) was too coarse to model effects from small inclusions like ferritin molecules with a radius around 4 nm,⁶³ we instead modelled iron-containing cells in *ii*) with a radius of approximately 0.5 μ m. We chose a volume fraction of $\zeta_s=0.05$, and an intrinsic spherical susceptibility of $\chi_s\approx 1100$ ppb, such that the bulk susceptibility in the

whole microstructure was $\overline{\chi}_s = \zeta_s \chi_s \approx 55$ ppb. The susceptibility, size and volume fraction could mimic dopaminergic cells containing e.g. ferritin and neuromelanin³, and may be found in WM near the Substantia Nigra³. Non-overlapping intra-axonal spheres were randomly packed using a previously designed packing generator¹⁴. We assumed the spherical cellular inclusions were impenetrable to water and their water signals fully relaxed, like myelin water. Again, we calculated the local Larmor frequency shift $\Omega(\mathbf{r})$ numerically⁶¹ using Eq. (1), with $\chi_s(\mathbf{r}) = \chi_s v_s(\mathbf{r})$ for the same 50 orientations of $\hat{\mathbf{B}}$.

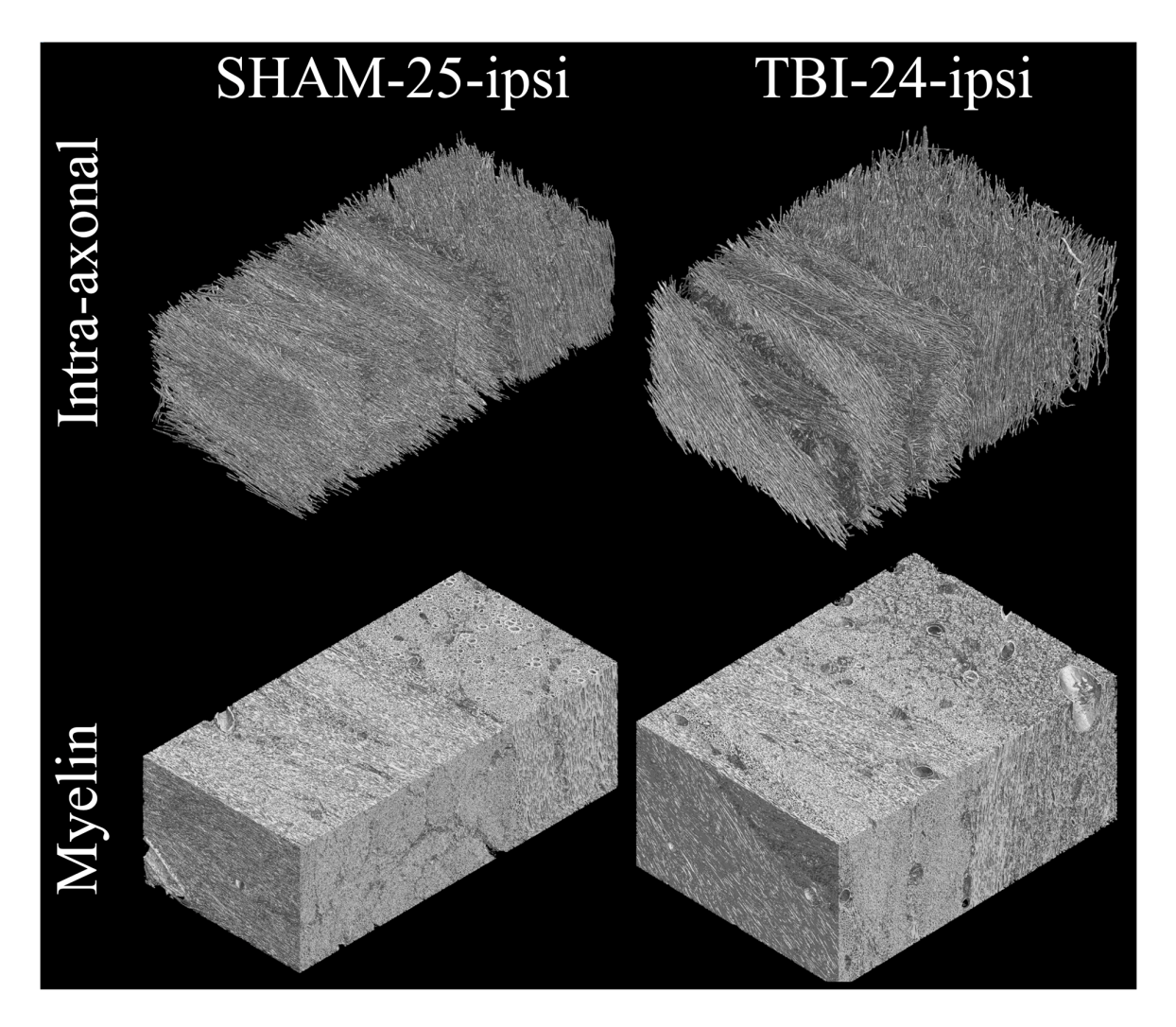


Figure 2 – Exemplary of in-silico white matter axon phantoms used for Monte-Carlo simulations. Eight different substrates from two different sham rats labelled 25 and 49 and two different TBI rats labelled 2 and 24 were used for Monte-Carlo simulations. Labels correspond to the original data^{64,65}. For each brain, both ipsilateral (ipsi) and contralateral (contra) tissue samples are considered. The tissue is extracted from the corpus callosum and cingulum bundles. The intra-axonal spaces are used

for the Monte-Carlo simulation of diffusing spins, while the myelin sheaths constitute the magnetizable tissue, perturbing the Larmor frequency of the diffusing spins.

Monte-Carlo simulations

We performed MC simulations in the major fiber bundle of each substrate to simulate an intra-axonal asymmetric spin-echo MRI signal (ASE) $S_{ASE}(T_E, \Delta T_E)$ with echo time T_E and delayed readout ΔT_E , and gradient echo $S_{MGE}(t)$ with gradient echo time t (here normalized). While details of the simulation framework are described in our previous publication¹², we give here the main details of the simulator: The MC simulations were restricted to intra-axonal spins. Each particle performed random steps drawn from a uniform distribution with a step length of $\delta_l = 0.1 \, \mu m$, matching the voxel resolution. The intrinsic diffusivity was set to 2 μ m²/ms, corresponding to a time step of $\delta_t = 0.83 \,\mu$ s. Steps crossing the intra-axonal boundary were rejected. The axon ends were prepared to allow fully periodic boundary conditions within the intra-axonal space, thereby avoiding artificial orientation dispersion. The MC simulations were used to simulate a multi gradient echo signal S_{MGE} (MGE), an asymmetric spin echo (ASE) signal S_{ASE} . Signal dephasing caused by the varying Larmor frequency $\Omega(r)$, was described by a normalized signal phase tensor $\varphi(T_E; p, t)$ for each random walker p, corresponding to each of the six independent tensor elements of the magnetic field tensor $\mathbf{A}(r) \equiv [\delta \chi \otimes \Upsilon](r)$, such that $\Omega(r) =$ $\gamma B_0 \widehat{\mathbf{B}}^{\mathrm{T}} \mathbf{A}(\mathbf{r}) \widehat{\mathbf{B}}$, and for each encoded echo time T_E : $\boldsymbol{\varphi}(T_E; p, t) = \xi_{T_E}(t) \boldsymbol{\varphi}(p, t - 1) + \delta_t \mathbf{A}(\mathbf{r}_p(t))$. Here the function $\xi_{T_E}(t)$ specifies when a 180-degree RF pulse (here an ideal phase flip) occurs and $r_p(t) = r_{p0} + \Delta r_p(t)$ denotes the position of the particle, where r_{p0} is the initial position and $\Delta r_p(t)$ the displacement. Numerically, φ was stored as an array with dimensions given by the total number of particles, number of echo times T_E and the 6 tensor components of **A**. For the MGE signal, $\alpha(t) = 1$ for all t and here we write the normalized signal tensor as $\varphi(p;t)$ for simplicity. The ASE signal $S_{\text{ASE}}(T_E + \Delta T_E)$ at a time $T_E + \Delta T_E$, where ΔT_E denotes the asymmetric delay after T_E , were computed for all combinations $\gamma B_0 \hat{\mathbf{B}}^{\mathrm{T}} \boldsymbol{\varphi} (T_E + \Delta T_E; p) \hat{\mathbf{B}}$ of $\hat{\mathbf{B}}$ and B_0

$$S_{\text{ASE}}(T_E, \Delta T_E) = \frac{1}{N} \sum_{p} e^{-\gamma B_0 \hat{\mathbf{B}}^{\text{T}} \boldsymbol{\varphi}(T_E + \Delta T_E; p) \hat{\mathbf{B}}} \quad \text{(ASE)},$$

$$S_{\text{MGE}}(t) = \frac{1}{N} \sum_{p} e^{-\gamma B_0 \hat{\mathbf{B}}^{\text{T}} \boldsymbol{\varphi}(p; t) \hat{\mathbf{B}}} \quad \text{(MGE)}.$$

(MC simulated MRI signals)

Each simulation used $N = 4 \times 10^6$ random walkers distributed uniformly across the axon bundle, with a computation time of approximately one day per substrate. The simulated signals for each protocol can also be written as

$$\begin{split} S_{ASE}(T_E, \Delta T_E) &= \exp \left(-\eta^{SE}(T_E) - \eta^{ASE}(T_E, \Delta T_E) - i \varphi^{ASE}(\Delta T_E) \right) \\ S_{MGE}(t) &= \exp \left(-\eta^{MGE}(t) - i \varphi^{MGE}(t) \right). \end{split}$$

Here η^{SE} , η^{ASE} , η^{MGE} are the sequence-dependent, dimensionless and time-dependent net signal decay functions caused by the heterogenous Larmor frequency shifts. Notice η^{ASE} depends also on the echo time T_E^{29-31} . We calculated the signal within each individual axon in the axonal substrate, where the induced field was generated by i) only the axonal sheath microstructure or ii) only intra-axonal spherical inclusions packed as in b).

The MGE signal was calculated at times t=0,2,4,...,18 ms, while the ASE signal was calculated at $T_E=20,22,24,...,40$ ms with asymmetric readout $\Delta T_E=0,2,3,...,20$ ms. Notice that the ASE signal is an SE signal when $\Delta T_E=0$ ms ($\eta^{ASE}(T_E,0)=0$), which meant that we could also extract the SE transverse relaxation from the same simulation. The external magnetic field strength was ${\bf B}_0={\bf B}_0{\bf \hat B}$, with ${\bf B}_0=3$ T, 7T or 16.4T along the same 50 different directions ${\bf \hat B}$.

For the total intra-axonal signal within the major fiber bundle, we estimated the transverse signal relaxation using $\eta^{MGE}(t) = -\ln(|S_{\rm MGE}(t)|)$, $\eta^{ASE}(\Delta T_E) = -\ln(|S_{\rm ASE}(\Delta T_E, T_E = 20~{\rm ms})|)$ and $\eta^{SE}(T_E) = -\ln(|S_{\rm SE}(0, T_E)|)$ for all ${\bf B}_0$. Similarly, in order to compare the net signal relaxation to the compartmental signal decay contributions in Eq. (4), we also estimated each compartmental signal decays η^{MGE}_a , η^{ASE}_a and η^{SE}_a and phases φ^{ASE}_a and φ^{MGE}_a . We chose the lowest simulated echo time $T_E = 20~{\rm ms}$ to maximize estimation accuracy of η^{ASE} .

First, we investigated if the orientation dependence of η^{SE} , η^{ASE} , η^{MGE} could be described by Eq. (8) for all echo times. Second, we tested if η^{SE} , η^{ASE} , η^{MGE} in a realistic bundle of coherently aligned axons is in fact described by the compartmental signal decays in Eq. (4), and if the scaling on time and B_0 is in agreement with short-range structural disorder⁴³ when $t \gg \tau$. This was done by comparing η^{SE} , η^{ASE} , η^{MGE} , at every time and B_0 strength, to the computed intra-axonal contributions $\overline{\eta}$, $\overline{\eta^2} - \overline{\eta}^2$ and $\overline{\varphi^2} - \overline{\varphi}^2$ c.f. Eq. (4) across all orientations $\widehat{\mathbf{B}}$. Hence, no fitting was involved. Besides confirming if the net signal decay could be captured by Eq. (4), it also enabled us to examine if the time and B_0 dependence follows our theoretical prediction: $\overline{\eta} \propto t^{-2\nu+2} (\gamma B_0 \chi)^2$, $\overline{\eta^2} - \overline{\eta}^2 \propto t^{-2\nu+4} (\gamma B_0 \chi)^4$ for $t \gg \tau$ and $\overline{\varphi^2} - \overline{\varphi}^2 \propto t^2 (\gamma B_0 \chi)^2$.

MRI Imaging

We also analyzed the orientation dependence of the apparent transverse relaxation rates R_2 of available datasets. R_2 relates to η when $\eta = tR_2$. Although this relation may not hold in general (as explained in the Introduction and Theory sections), it can still be used to assess orientation dependence, provided that the functional form of η with respect to time does not vary across orientations. Equation (8) is therefore applicable to describe orientation dependence of R_2 , and the amplitudes a, b and c represent weighted averages of each parameter over all echo times used for estimating R_2 .

One dataset was acquired by Sandgaard et al.¹¹ and contains multi-gradient echo data and dMRI data at 9.4T from rat brain imaged at multiple sample orientations (details can be found in the paper). The second and third datasets examined were acquired by Aggarwal et al.⁴² for studying transverse relaxation in fixed human brain stem at 11.7T, and by Denk et al.³⁵ studying in vivo human brain WM. Transverse relaxation data vs. fiber direction was extracted from Aggarwal et al.⁴² and Denk et al.³⁵ using the online graph reader <u>automeris.io</u>. For the dataset by Sandgaard et al.¹¹ we fitted the apparent relaxation rate for each sample orientation for every individual voxel in a manually segmented region of Corpus Callosum (CC). The voxel-wise relaxation rates were then fitted to Eq. (8) using the main WM axon orientation determined from the main eigenvector of the fODF scatter matrix (see previous study¹¹ for details). Using Eq. 8 directly on all data means that we assume an axially symmetric fODF across all voxels, and that we neglect the effect of biological variation across the different voxels (see discussion on limitations and future studies).

5 Results

For clarity of presentation, we show here results for two substrates, sham-ipsi-25 and TBI-24-ipsi, as results were comparable across all substrates, including differences between sham and TBI rats.

In supplementary material S1, we show that the Larmor frequency variance from individual axons, both realistic and synthetically grown, respectively. Our simulation shows that none of the simplistic axons are close to the orientation dependence observed for the realistic axons, which means that all structural features are important when modeling relaxation in axons. Second, in supplementary material S2, we show that the magnetic field variance acquires a non-negligible contribution from neighboring axons. This means that not only must axons be modeled realistically, but the magnetic field induced by the whole microstructure must be considered.

Transverse relaxation inside realistic axonal microstructure

We start by considering the signal decay inside each individual axon, as they describe the three terms in Eq. (4) for ASE and MGE, and the two terms on Eq. (5) for SE. Figure 3-Figure 5 show the average

intra-compartmental decay $\overline{\eta}$, and inter-compartmental variances $\left(\overline{\eta^2}-\overline{\eta}^2\right)/2$ and $\left(\overline{\varphi^2}-\overline{\varphi}^2\right)/2$. All plots are shown for a fixed B_0 orientation and different echo times. $\overline{\eta}$ and $(\overline{\varphi^2} - \overline{\varphi}^2)/2$ are scaled by $(7T/B_0)^2$, for the three field strengths, to easily visualize if they scale as B_0^2 . The fourth order term $(\overline{\eta^2} - \overline{\eta}^2)/2$ is similarly scaled by $(7T/B_0)^4$. For axons (i), we find that $\overline{\eta}$ scales approximately as $t^{3/2}$ and B_0^2 , in agreement with 1D short range structural disorder and the signal decay being well described by the second signal cumulant. For the spheres (ii), the contribution depends on field strength and acquisition type: At 16.4T (squares markers in Figure 3-Figure 5), the term $\overline{\eta}$ for spheres deviates from $t^{3/2}$ and B_0^2 , especially for the ASE aquitition, and less for MGE and SE signals. However, at 3T and 7T (round and diamond shaped markers in Figure 3-Figure 5), $\overline{\eta}$ are in good agreement with $t^{3/2}$ and B_0^2 due to 1D short range structural disorder. The inter-compartmental variance $(\overline{\eta^2} - \overline{\eta}^2)/2$ did not contribute to the signal decay for axons (i), while for the spheres (ii), a small contribution was found to add to the net signal decay. The phase variance $(\overline{\varphi^2} - \overline{\varphi}^2)/2$ scale as t^2 for axons (i) and agreed with the spatially averaged Larmor frequency shifts $t^2 \left(\overline{\Omega^2} - \overline{\Omega}^2\right)/2$ (green line) estimated directly from the induced magnetic field variance. For the sphere-filled axons (ii), the phase variance $(\overline{\varphi^2} - \overline{\varphi}^2)/2$ agreed with $t^2(\overline{\Omega^2} - \overline{\Omega}^2)/2$ for 3T and 7T, while at 16.4T, the first order cumulant failed to explain each compartments' signal phase across all echo times.

These results show that the intercompartmental variance $\overline{\varphi^2} - \overline{\varphi}^2$ in phase shifts may be important when characterizing the net transverse relaxation across multiple compartments. Having gone through the signal decay from individual axons, we now consider the results for the net signal decay η^{SE} , η^{ASE} , η^{MGE} from all axons.

Figure 6Error! Reference source not found. shows η^{SE} , η^{ASE} , η^{MGE} for a fixed B_0 orientation and different echo times. The three decay functions are scaled by $(7T/B_0)^2$ for the three field strengths simulated for easy visualization, if η^{SE} , η^{ASE} , η^{MGE} scale as B_0^2 . All the net relaxation decays exhibit a clear time dependence that could not be captured by either a purely linear or a purely quadratic function of time. The axonal transverse relaxation (i) scales as B_0^2 , but slower in the presence of spheres (ii). This indicates that the net signal decay of axons is well described by the signal's second order cumulant, and that all three relaxation functions scale as $(\gamma B_0 \chi)^2$, except for the sphere-filled axons.

Figure 7Error! Reference source not found. shows the net decay of the "apparent" relaxation rates η^{SE}/T_E , $\eta^{ASE}/\Delta T_E$, η^{MGE}/t , for a fixed echo time and different B_0 orientations. We divide by time to make the units 1/s, to make it more intuitive. We fit all the net decays to Eq. (8) (black line) and found that the orientation dependence was well captured by this expression. The relaxation rate is lowest for SE, and the absolute difference across orientations decreased, as expected, which stems from a slightly

reduced intra-compartmental relaxation (cf. Figure 3-Figure 5) and because $(\overline{\varphi^2} - \overline{\varphi}^2)$ are refocused by the SE pulse sequence.

Using the individual axonal decays, shown in Figure 3-Figure 5, we also compute the expected net decay from Eqs. (4) and (5) (green lines in Figure 7). Here we find that the net signal decays η^{SE} , η^{ASE} , η^{MGE} can be described by the compartmental cumulant expansion up to second order (i.e. summing over compartments) even though the intra-compartmental signal decay η_a and phase φ_a from within each sphere-filled axons may be influenced by higher order cumulant (i.e. when summing over spins inside each compartment). This is true for all echo times. A clear difference in orientation dependence can be seen between sham and TBI for the axons. This is indicative by the decay curve across orientation having a minimum at a higher angle for TBI compared to sham. Looking at our simulations in the synthetic axons in supplementary material S1, this difference likely comes from increased beading in the diseased tissue, as demonstrated in a previous study⁶⁶.

In general, the rather sparse distribution of strongly magnetized spheres generates a substantially higher signal decay rate (around 10 times higher) than the myelinated axons, even though their bulk susceptibility was 50% lower than the axons. This shows that intrinsic susceptibility χ (roughly ten times higher for the spheres in our simulations) can be more important than the bulk susceptibility $\overline{\chi}$ for transverse relaxation.

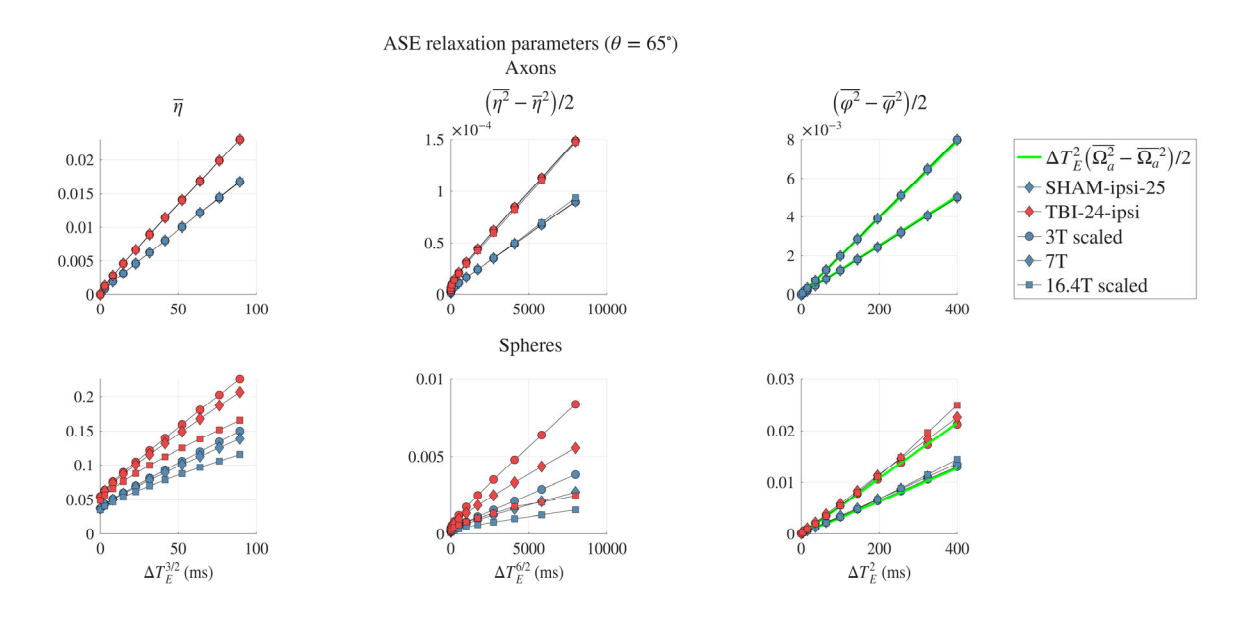


Figure 3 - Fitting parameters from fitting the ASE signal decay to the magnetic field variances for different echo times ΔT_E (Eq. (4)). Colors correspond to 2 different axonal substrates. The first row shows the contribution induced by the full EM axonal microstructure at three different B0 field strength indicated by the marker shape, while the bottom for spheres. The relaxation parameters are

scaled by $(7T/B_0)^2$. The green lines in the third column show the estimated phase variance from the induced magnetic field variance $\Delta \mathbf{B}$.

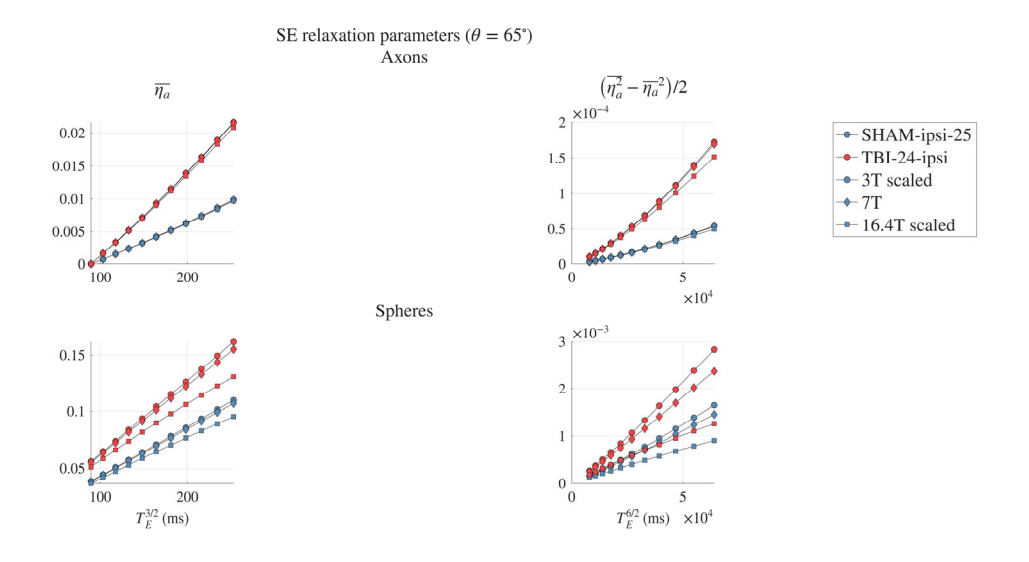


Figure 4 - Fitting parameters from fitting the SE signal decay to the magnetic field variances for different echo times T_E and $\Delta T_E = 0$, (Eq. (5)). Colors correspond to 2 different axonal substrates. The first row shows the contribution induced by the axonal microstructure at three different B0 field strengths as indicated by the marker shape, while the bottom is for sphere-filled axons. The relaxation parameters are scaled by $(7T/B_0)^2$.

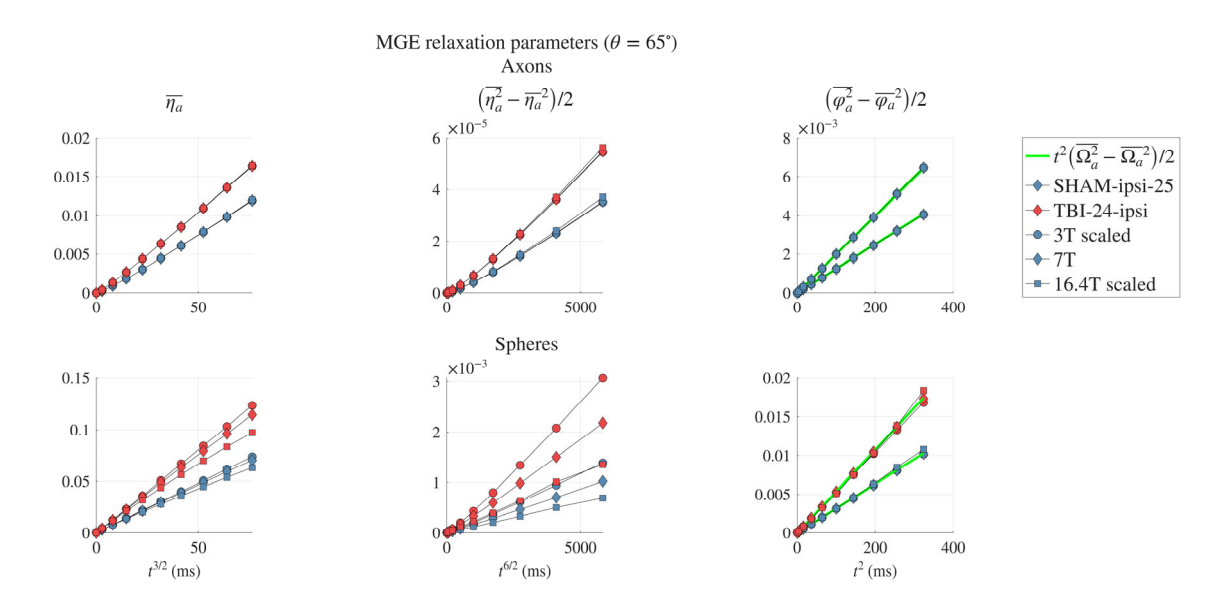


Figure 5 - Fitting parameters from fitting the MGE signal decay to the magnetic field variances for different echo times t, (Eq. (4)). Colors correspond to 2 different axonal substrates. The first row shows the contribution induced by the axonal microstructure at three different B0 field strengths as indicated by the marker shape, while the bottom is for sphere-filled axons. The relaxation parameters

are scaled by $(7T/B_0)^2$. The green lines in the third column show the estimated phase variance from the induced magnetic field variance $\Delta \mathbf{B}$.

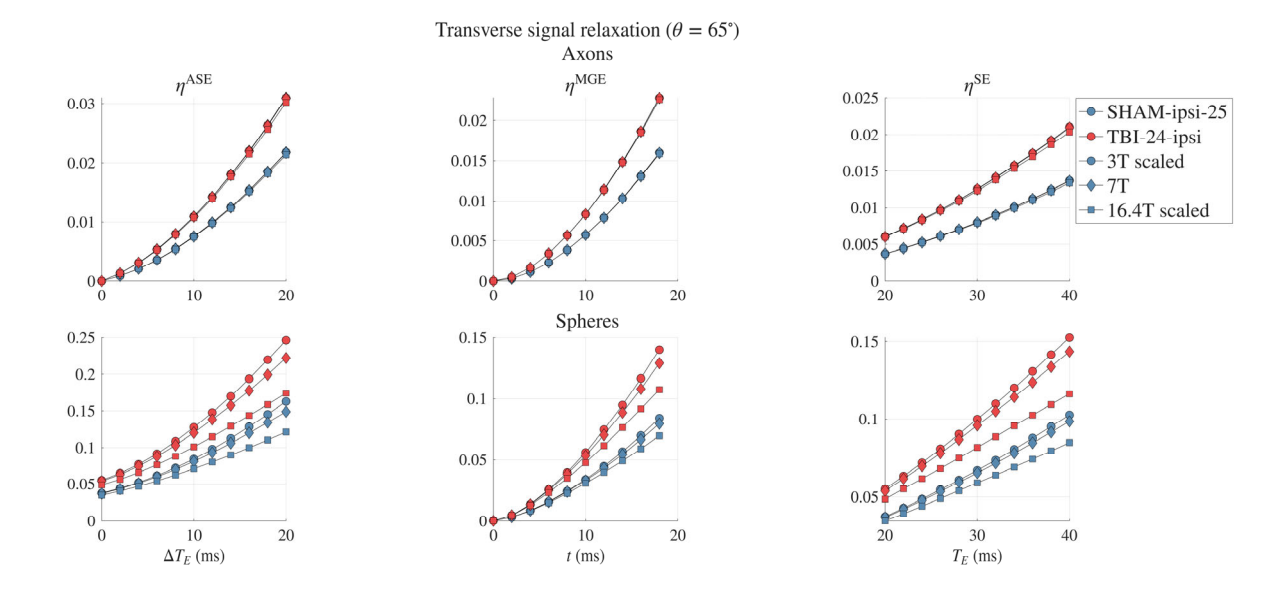


Figure 6 - Time dependent signal decay for an asymmetric spin-echo (ASE) and multi-gradient echo (MGE) signal plotted against echo time. Colors correspond to 2 different axonal substrates. The external field is oriented 65 degrees to the main fiber direction. The first row shows the signal relaxation induced by the unmodified EM axonal microstructure at three different B0 field strength. The signal decay parameters are scaled by $(7T/B_0)^2$. Bottom row shows the relaxation induced by spheres. Black lines indicate power law fitting.

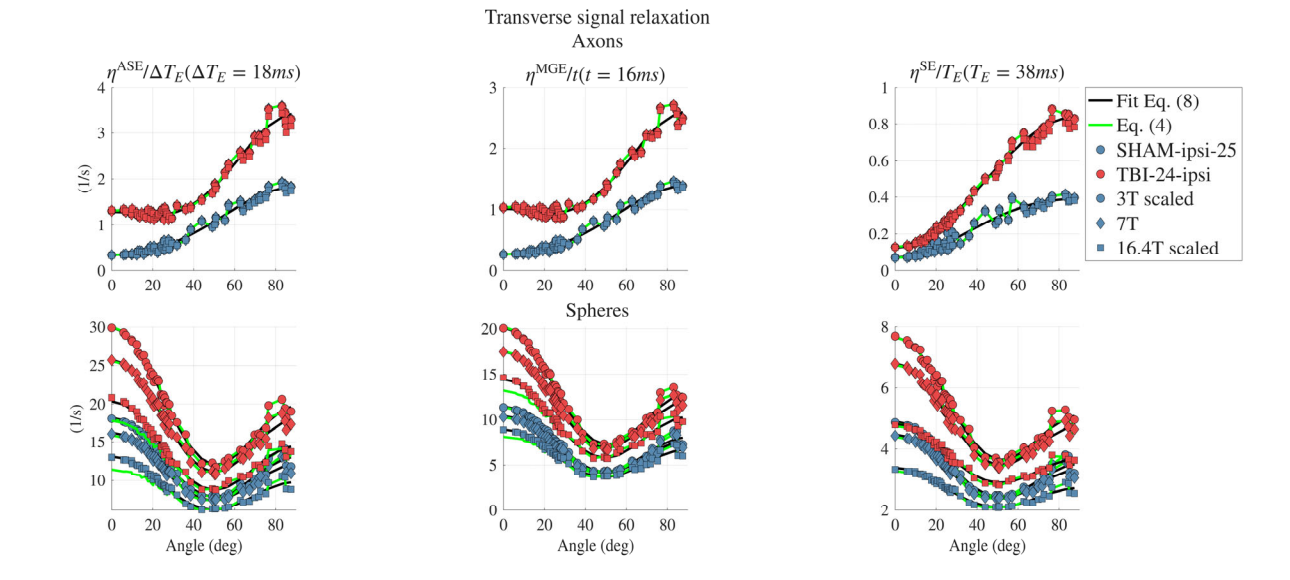


Figure 7 - Transverse relaxation for spin-echo (SE), asymmetric spin-echo (ASE) and multi-gradient echo (MGE) signals plotted against the angle between the external field and the main fiber bundle at a fixed echo time. Colored points correspond to 2 different axonal substrates. The first row shows the relaxation induced by the realistic axonal microstructure at three different B0 field strength. The relaxation parameters are scaled by $(7T/B_0)^2$. Bottom row shows the relaxation induced by spheres. Black line shows fitting to Eq. (8) and the green line estimated from Eq. (4) for MGE and ASE and Eq. (5) for SE.

MRI Imaging

Figure 8 shows the transverse relaxation rate R_2 in WM tissue voxels from three different imaging studies. Overall, Eq. (8) could explain the main orientation dependence of all three studies. Table 1 shows the fitting amplitudes. The relaxation rate clearly scales with B_0 , and the anisotropic amplitudes a, b are in better agreement with B_0^2 than B_0 . However, given the substantial variability arising from biological differences across WM tracts, animal type, and echo times, a clear scaling relation cannot be established at this stage and warrants further investigation.

Table 1 – Amplitudes from fitting MRI data to Eq. (8)

Fitting amplitudes	B_0	Type	Fixation	Tissue	а	b	С
(1/s)							
Denk et al.	3T	Human	In vivo	Whole brain	4.4	6.5	22
Sandgaard et al.	9.4T	Rat	Ex vivo	Corpus Callosum	20	27	51

Aggarwal et al.	11.7T	Human	Ex vivo	Transverse Pontine fibers	33	47	66
Aggarwal et al.	11.7T	Human	Ex vivo	Corticospinal tract	39	61	74

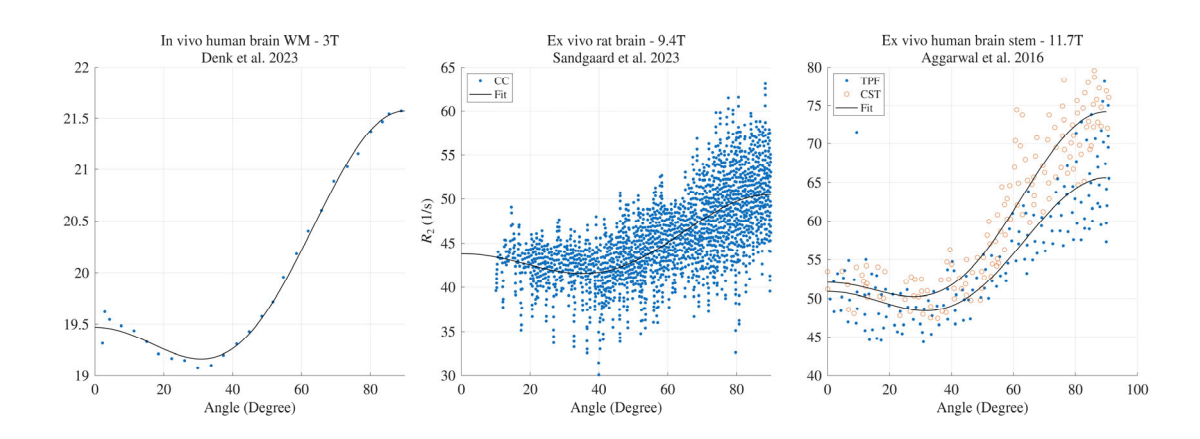


Figure 8 - Left: Transverse relaxation in in vivo human white matter at 3T. Angles denotes the angle between B0 and the major eigenvector of the diffusion tensor **D** from DTI. Middle: Transverse relaxation in an ROI of corpus callosum from an ex vivo mouse brain imaged at 9.4T. Each point corresponds to a voxel and the angle was found as the angle between B0 and the major eigenvector of the fODF scatter matrix **T**. **T** was estimated using Fiber Ball Imaging⁶⁷ (FBI). Right: Transverse relaxation in human brainstem at 11.7T. TPF denotes transverse pontine fibers while CST are corticospinal tracts. Angles was estimated by the angle between B0 and the major eigenvector of the diffusion tensor **D** from DTI.

6 Discussion

Towards a complete model of WM transverse relaxation rate

Orientation and time dependence of WM transverse relaxation

In this work, we studied the orientation dependence of the magnetic field variance and transverse relaxation in realistic white matter magnetic microstructure. We argued theoretically that the orientation dependence in an axially symmetric and translation invariant microstructure involves only even order cosines up to 4th order. We also expect our results to remain a good approximation in nearly axially symmetric cases, presumable widespread across the brain. Our Monte-Carlo simulations were also carried out inside axonal bundles, which were part of larger WM substrates (cf. Figure 2) containing

multiple bundles oriented with no axial symmetry. This demonstrates that the orientation dependent MR signal relaxation in voxels containing different oriented WM tracts should not be modelled directly using Eq. (8), but instead by using Eqs. (10)-(11), where the fiber orientation distribution (fODF) captures the non-axially symmetric orientating of the WM tracts, and the signal relaxation from a single tract are described by Eq. (8). Hence, our work showed that microstructure alone can account for the orientation functional dependence previously ascribed to intrinsic susceptibility anisotropy³⁶. We validated our results by numerically computing magnetic field variations induced by realistic axonal substrates obtained from electron microscopy, and by additional spherical inclusions added by hand inside the axons. Our theoretical derivation assumed the field perturbations were weak enough for the signal decay to be well described by the second signal cumulant. When the intra-compartmental signal decay is too strong for the cumulant expansion up to second order to remain valid - as indicated by a decay rate that does not scale with B_0^2 such as in the presence of the spheres – more cumulants may need to be considered to describe its signal decay, or perhaps be in better agreement with strong static dephasing defined by $\sigma_c \tau$, $t/\tau \gg 1$, 55. Previous results for the transverse relaxation in the strong static dephasing regime of randomly positioned spheres derived a dependence on the absolute mean of the Larmor frequency shift⁹. As the absolute mean of the Larmor frequency shift in our simulation was found to depend on second order cosines¹², we expect Eq. (8) also hold for static dephasing in an axially symmetric microstructure, which may be why we could explain the orientation dependence even when the compartmental signal phase was insufficiently described by the first signal cumulant. Interestingly, our simulations showed that the second order cumulant expansion across compartments (capturing intercompartmental differences in signal decay and phase) proved valid in describing the net signal, but that the second order cumulant expansion of the intra-axonal signal failed in describing the intracompartmental signal phase induced by the magnetized spheres at ultra-high field (16.4T). Properly describing the intra axonal signal phase may therefore require including the third order cumulant, or accounting for strong static dephasing. This will be investigated in the future.

Besides orientation dependence, we also investigated the time dependence of the signal decay with our Monte-Carlo simulations and found that 1D short-range structural disorder described our findings for axons, while spheres agreed with short-range disorder, when the field strength and echo times were sufficiently small.

We found that TBI increased the transverse signal relaxation and resulted in a different orientation dependence compared to sham. This difference could be induced by morphological features such as axonal beading (see simulation in Supplementary S1). A recent study⁶⁶ using the same axonal substrates found that TBI increases the cross-sectional variance from e.g. enhanced beading, which from the point of view of transverse relaxation would increase the dipolar-like contribution – in agreement with our findings. In Figure S6Error! Reference source not found., we see that TBI-ipsi in C3-C5 (individual axons with different structural features cf. Figure 2) had a higher dipolar modulation, which based on

simulations in Supporting material S1 indicates a higher axonal sinuosity, in agreement with the previously mentioned study⁶⁶. Compared to the structurally modified axons, C2 to C6, indicates that beading along the axis is more important than non-circular cross-sections, as the magnetic field variance changed the most when beading was removed.

Scaling of magnetic susceptibility in WM signal

The transverse signal relaxation η from myelinated axons was in good agreement with the prediction from the second signal cumulant, scaling with field strength to the second power, as seen in Figure 7Error! Reference source not found. Error! Reference source not found.. This means that transverse relaxation from myelinated axons in our simulations should scale with $\zeta_m\chi_m^2$ for the considered range of χB_0 values, which we believe encompasses a wide span of realistic conditions. For spherical perturbers, neither a linear nor a squared scaling relation of magnetic susceptibility was adequate for explaining all the simulations across all the 8 substrates. In practice we found from the 3T and 7T simulations that when χB_0 was sufficiently low, the transverse relaxation scaled approximately as B_0^2 , and thus as $\zeta_s \chi_s^2$, and as the field strength increases, the exponent of the scaling decreased. This means that the apparent scaling exponent depends on the experimental setup and iron content. It is therefore important to match the correct model to the experimental design, and the best model may be different in iron-deficient WM such as the Corpus Callosum compared to WM near the substantia Nigra or more superficial WM^{3,4,68}. In practice, estimating and distinguishing such scaling exponents of magneticsusceptibility-induced relaxation is challenging, not only because identifying the correct power law in time is inherently difficult, but also due to practical limitations such as the need for several orders of magnitude in dynamic range, and a strong dependence on the earliest time points. Identifying the correct power law may therefore be hard with finite and noisy data sets and further compounded by the presence of biological variability.

Limitations

Contribution from point-like spherical sources

In our simulations, spherical inclusions had a radius comparable to the axons, as smaller spheres gave numerical errors in the computed magnetic fields. Hence, we could not simulate the effect of strongly magnetized point-like particles. For example, ferritin molecules have a diameter around 4 nm and magnetic susceptibility 520 ppm⁶⁹. In comparison, our resolution was 0.1 µm in the axonal substrates. A voxel containing one ferritin molecule would thus have an effective susceptibility around 140 ppb. This means that our simulation resolution prevented us from probing strong frequency shifts induced by point-like particles. Instead, we focused on larger spheres to mimic iron-containing cells.

Another limitation was that we only packed intra-axonal cells/spheres and simulated intra-axonal MC signals. We believe this is sufficient for our study because if iron is mainly in neuroglia or axonal mitochondria²⁴, the magnetic field inside a single axon caused by iron-containing spheres elsewhere in the tissue can barely distinguish whether those spheres are located in other axons or in the extra-axonal space. Hence, we believe it is sufficient to pack spheres only in the intra-axonal space, which made the time it took to pack the spheres more feasible, and we did not have to consider how accurately the extra-axonal space was segmented. Simulating the extra-axonal signal will however be considered in future studies. But, based on our investigation of the Larmor frequency variance (cf. Error! Reference source not found.), which was larger in the extra-axonal space across all substrates, we expect the transverse relaxation rate to be faster outside than inside the axons, and that extra-axonal spheres would give a rise to similar time- and orientation-dependents effects, if packed with similar volume fraction.

Beyond the modelled orientation dependence

While our results are especially applicable to ex vivo tissue, the situation in vivo is more complex: Transverse relaxation arises not only from magnetic field variations induced by the magnetized microstructure, but also from additional mechanisms. For instance, molecular relaxation contributes both ex vivo and in vivo, is most likely orientation independent, and increases linearly with time⁵⁵. Such relaxation will contribute to the orientation-independent amplitude c in Eq. (8). Recent work has nevertheless indicated the presence of orientation-dependent relaxation²⁶, arising from dipole-dipole interactions between water and the myelin sheath – the so-called THB model. The THB model explains orientation-dependent relaxation as arising when a water proton transiently forms a hydrogen bond with an ordered (anisotropic) macromolecular proton pool. If the interaction strength is sufficiently high, the relaxation becomes largely independent of B_0 strength. As an example, provided by the authors: assume that a sufficient fraction of water molecules participates in these events (around 10%) at every moment. If a proton remains in the transiently bound state for an average lifetime of approximately 10 to 60 ns, during which it experiences a strong dipolar interaction around 20 $(s \cdot ns)^{-1}$, the net relaxation rate ranges between 1-4 1/s to 10-35 1/s, respectively, depending on the orientation but independent of field strength commonly used in MRI. The minimum relaxation rate will be around 42 degrees. Disentangling the respective contributions from THB and microstructure in realistic white matter will require carefully designed experiments capable of isolating each effect, which we aim to pursue in future work.

On a microscopic scale, cardiac pulsations may further introduce time- and orientation-dependent transverse relaxation, modulated by blood vessel size. In line with these multiple contributing factors, recent work in gray matter has demonstrated that it may be possible to disentangle heme and non-heme

relaxation⁷⁰, suggesting that a similar approach could help to separate different sources of transverse relaxation in WM as well.

Experimental discrepancies

The proposed orientation dependence of the transverse relaxation rate could describe the experimental findings investigated. However, other in-vivo studies in brain WM, using the principal eigenvector of the diffusion tensor as a proxy for the orientation of the axonal microstructure, found that the relaxation rate had a large dipolar contribution but with a minimum rate around 20 degrees compared to 30 degrees in the studies considered here (cf. Figure 8). This exact combination of angle minima and dipolar-like modulation cannot be explained by Eq. (8). But, Denk et al. ⁴⁰ found that venous blood vessel do not necessarily follow the direction of the axons, and this can introduce an offset in the relaxation rate angular dependence. Denk et al. also demonstrated that anisotropic voxel shapes can elevate the effect of venous blood on transverse relaxation. This is why we limited our experimental comparison to studies with isotropic voxel resolution. Hence, we do not see this discrepancy as a disagreement with our work. In addition, introducing an angle-offset to Eq. (8), we can describe said studies⁴⁰ with such a lower angle minimum. We also emphasize that a voxel's signal includes convolution with a fiber orientation distribution due to orientation dispersion. In human WM, orientation dispersion is ever-present^{48,49} and can include crossing fibers⁷¹ etc. and such effects should not be neglected. Eq. (8) should therefore only be used directly to describe the voxel transverse relaxation rate when the fODF is axially symmetric.

A limitation of the present MRI datasets is that multiple voxels were used to examine orientation dependence. Since WM voxels may differ biologically across tracts, this introduces potential bias. A more rigorous assessment would require a carefully designed experiment on the same tissue sample, acquired at identical echo times but under different orientations and field strengths, to fully avoid confounding tissue variations. Such an experiment could provide clearer insights into both orientation and time dependence and will be carried out in the future.

Propositions for transverse relaxation modelling and susceptibility estimation

Quantitative Susceptibility Mapping (QSM) has been combined with models of transverse relaxation to disentangle dia- and paramagnetic contributions from e.g. myelin and iron in the brain^{32,33,70}. Our results here challenge the interpretability of susceptibility values obtained from susceptibility models combining phase and transverse relaxation, and such models should be used with caution. This is because an assumption in such models is that both sources (myelin and iron) contribute to the MR signal under a static dephasing regime, particularly at long echo times where the signal can no longer be accurately described by a Taylor expansion. Under this assumption, transverse relaxation is expected to scale linearly with the bulk susceptibility $\overline{\chi}$ and thus with myelin and iron concentration - and with the main magnetic field B_0 . However, our simulations did not support the presence of a strong static

dephasing regime for myelinated axons; instead, the transverse relaxation scaled non-linearly with time, corresponding to short-range structural disorder. As the transverse relaxation for myelin scaled as B_0^2 , it must also scale as χ^2 with the intrinsic magnetic susceptibility, as varying B_0 is indistinguisable from varying χ (cf. Eq. (1)). Moreover, axons induced substantially lower transverse relaxation rates than spherical inclusions in our simulations, despite spheres having a lower bulk susceptibility, which may complicate the estimation of myelin content in the presence of non-negligible relaxation induced by iron. For spheres, the relaxation rate did not conform strictly to either a linear or quadratic scaling, but somewhere in between. Even if an appropriate scaling relationship were identified for each source, the absolute relaxation rates remain highly dependent on microstructural morphology, and orientation dependent higher-order correlations between the two magnetic sources are also present which may lead to additional complexity in describing the transverse relaxation.

Hence, our work highlights a major challenge of using the transverse relaxation rate directly for susceptibility estimation. Nevertheless, it demonstrates that time and orientation independent relaxation parameters can still be identified and that these reflect underlying morphology and magnetic properties, thereby potentially providing biomarkers for neurodegenerative diseases. In this respect, our results agree with Winther et al.³⁴ findings on the effect of axonal morphology on transverse relaxation. Here we extended their results by showing that the whole microstructure must be considered when describing the signal's transverse relaxation.

Overall, we propose to describe the measured MRI signal similarly to the Standard Model of WM⁵⁰, where a mesoscopic signal kernel is convolved with a fiber orientation distribution function (fODF). Our model may be unified with SM such that diffusion weighting can be used to disentangle signals from the intra- and extra-axonal spaces, but also to probe the orientation dependence of both transverse relaxation and Larmor frequency shifts without sampling the MRI at multiple B_0 orientations⁷². Merging diffusion and susceptibility modelling, to improve parameter estimating, is an on-going study⁷² and will be presented in the future.

7 Conclusion

We demonstrated that realistic white matter substrates containing myelinated axons and spherical inclusions induce orientation- and time-dependent transverse relaxation. Signal dephasing caused by myelinated axons follows a quadratic dependence on susceptibility and field strength, whereas spherical inclusions, such as iron-rich neuroglia, can produce strong relaxation effects that deviate from this simple power-law. However, the time-dependent power-law signature arising from structural disorder in white matter is weak and may be difficult to detect at currently achievable noise levels, echo times, and field strengths, because the power-law curvature over typical echo times deviates only slightly from

a linear trend. Transverse relaxation varied by several Hz depending on orientation and B_0 field, making it more feasible to measure, as demonstrated with actual MRI data.

These findings challenge current models for estimating magnetic susceptibility from multiple sources and highlight the importance of accounting for both microstructural geometry and compartment-specific magnetic properties in modeling transverse relaxation. Incorporating both time- and orientation-dependent effects may provide more robust biomarkers of tissue pathology, less biased by experimental conditions. Future work will focus on extending this framework to include diffusion-weighted imaging, with the goal of enabling more accurate in vivo characterization of white matter microstructure and its alterations in disease.

8| Funding

This study is funded by the Independent Research Fund Denmark (Grant Number 10.46540/3103-00144B).

9 Competing interests

The author(s) declare no competing interests.

10 Author Contributions

Anders Dyhr Sandgaard: Conceptualization, Methodology, Software, Formal analysis, Investigation, Writing - Original Draft, Visualization.

Rafael Neto Henriques: Methodology, Writing - Review and Editing,

Noam Shemesh: Methodology, Resources, Writing - Review and Editing,

Sune Nørhøj Jespersen: Conceptualization, Methodology, Writing - Review & Editing, Supervision, Project administration, Funding Acquisition

11 Availability of data

The code used to process the data, calculate the magnetic fields, and perform MC simulations is available upon reasonable request to the corresponding author.

12| Symbols

 \hat{n} : Cylinder direction vector

 $\mathcal{P}(\widehat{\boldsymbol{n}})$: Fiber Orientation Distribution Function

T: Mean orientation tensor of cylinder directions \hat{n} . Relates to second moment of $\mathcal{P}(\hat{n})$

 χ : Magnetic Susceptibility

 $\mathbf{B}_0 = \widehat{\mathbf{B}}B_0$: Magnetic field vector with direction $\widehat{\mathbf{B}}$ and magnitude B_0

 θ : Angle between $\hat{\mathbf{B}}$ and $\hat{\boldsymbol{n}}$

 $\xi(t)$: Spin-flip function describing the signal encoding protocol

V: Macroscopic (voxel) volume

 \mathcal{M} : Mesoscopic volume

 $b, \hat{\mathbf{g}}$: Diffusion encoding

 l, τ, D : Correlation length of microstructure, correlation time $\tau = l^2/D$, where D is diffusivity

v = p + d: Dynamical exponent of microstrucutre, where p denotes the structural disorder class and d the effective dimension of diffusion process.

 $\eta(t)$: Transverse relaxation decay function of signal

 γ : Gyromagnetic ratio of water.

 $\Upsilon(r)$: Dipole field tensor

 $\Delta \mathbf{B}(\mathbf{r})$: Induced magnetic field of tissue

 $\Omega(\mathbf{r})$: Local Larmor frequency shift induced by $\Delta \mathbf{B}(\mathbf{r})$

 $\varphi(t)$: Signal phase at time t induced by $\Delta \mathbf{B}(\mathbf{r})$

 f_c : Signal fraction of compartment c in volume V

 Ω_c : Intra-compartmental mean Larmor frequency shift $\Omega(r)$ in compartment c

 σ_c^2 : Intra-compartmental variance of Larmor frequency shift $\Omega(\mathbf{r})$ in compartment c

(...): Averaging across spins

 $\overline{(...)} = \sum_{c} f_{c}$ (...): Averaging across compartments c with signal fraction f_{c}

 $\overline{\Omega} = \sum_c f_c \, \Omega_c$: Inter-compartmental mean of intracompartmental mean Larmor frequency shift Ω_c

 $\overline{\sigma^2} = \sum_c f_c \, \sigma_c$: Inter-compartmental mean of intracompartmental variance of Larmor frequency shift

 $\overline{\varphi} = \sum_c f_c \, \varphi_c$: Inter-compartmental mean of intracompartmental phase φ_c

 $\overline{\Omega^2} - \overline{\Omega}^2$: Inter-compartmental variance of Mean Larmor frequency shift Ω_c

 $\overline{(\sigma^2)^2} - \left(\overline{\sigma^2}\right)^2$: Inter-compartmental variance of intracompartmental variance of Larmor frequency shift ς_c

 $\overline{\varphi^2} - \overline{\varphi}^2$: Inter-compartmental variance of intracompartmental phase φ_c

a(t), b(t), c(t): Fitting amplitudes of $\eta(t)$ versus the angle θ

v(r): Spatial indicator function

 ζ : Volume fraction of v in volume \mathcal{M}

t: gradient echo time

 T_E : Spin echo time

 ΔT_E : Delayed time after T_E of signal read-out

 \mathcal{K} : Signal Kernel for a bundle of parallel sticks

13 Supplementary Materials captions

Figure S1 - Overview of synthetic axons filled with randomly packed spheres. A tube with randomly varying radius was generated and each cross-section of the tube was shifted randomly in the radial direction by an amount L_{shift} . First two rows show the tube filtered by a 3D Gaussian filter, where the first two collumns show the tube before smoothing, and the last two rows after smoothing. First row shows without any shift L_{shift} , while the second shows with shift. The second and third rows show axons with 2D Gaussian smoothing perpendicular to the axon, and the latter two rows with 1D smothing longitudinally.

Figure S2 - Larmor frequency variance induced by synthetic axonal myelin sheath with scalar susceptibility. First six rows show the intra-axonal magnetic field variance for 3D, 2D or 1D Gaussian smoothing and cross-sectional shift L_{shift} . The last six rows show variance outside the synthetic axons. X-axis denotes the angle between B0 and axon.

Figure S3 - Larmor frequency variance induced by randomly packed spheres with scalar susceptibility inside a synthetic axon. First six rows show the intra-axonal magnetic field variance for 3D, 2D or 1D Gaussian smoothing and cross-sectional shift L_{shift} . The last six rows show variance outside the synthetic axons. X-axis denotes the angle between B0 and axon.

Figure S4 - Parameters of Eq. (8) after fitting Larmor frequency variance induced inside synthetic axon generated by either the synthetic axons or by randomly packed sphered in the axons. Here is shown for a radius $R_S/R_0=0.25$ for the spheres compared to the mean axon radius. X-axis denoted the amount of cross-section shifts induced for each axon slice, while the y-xais the size of the

smoothing filter. First two rows show for 3D Gaussian smoothing, the next two 2D Gaussian smoothing and the latter rows 1D Gaussian smoothing. Colors are clippped in order to visualize the whole range of values.

Figure S5 - In-silico white matter axon phantoms used for Monte-Carlo simulations. Eight different substrates from two different sham rats labelled 25 and 49 and two different TBI rats labelled 2 and 24 were used for Monte-Carlo simulations. Labels correspond to the original data. For each brain, both ipsilateral (ipsi) and contralateral (contra) tissue samples are considered. The tissue is extracted from the corpus callosum and cingulum bundles. The intra-axonal spaces are used for the Monte-Carlo simulation of diffusing spins, while the myelin sheaths constitute the magnetizable tissue, perturbing the Larmor frequency of the diffusing spins.

For each substrate, we considered the magnetic field variance induced by each axon. In the spirit of Winther et al.³⁴ we synthesized 6 different axons with varying microstructural features to investigate the intra-axonal and extra-axonal magnetic field average and variance. Labeling was kept as in Winther et al. for consistency.

Figure S6— Larmor frequency variance induced by individual axonal myelin sheaths or intra-axonal spherical sources (C5 spheres) versus the angle between B0 and average direction of the axon. First three rows show the variance inside every axon, while the last row shows extra-axonal variance. Labels (C2-C6) indicate the diffent morphological features considered (see Figure 2). Each line shows results for 2 different WM substrates, including fits and minima.

Figure S7 - Larmor frequency variance, induced by axonal myelin sheaths with scalar susceptibility, versus angle between B0 and the average direction of the major fiber bundle. First row shows the intra-axonal variance for 2 different WM substrates, with the first column displays the variance in the extra-axonal space. Second row shows the variance by intra-axonal spherical sources with scalar susceptibility.

14 References

- Xu T, Foxley S, Kleinnijenhuis M, Chen WC, Miller KL. The effect of realistic geometries on the susceptibility-weighted MR signal in white matter. *Magn Reson Med*. 2018;79(1):489-500. doi:10.1002/mrm.26689
- 2. Lee J, Shmueli K, Kang BT, et al. The contribution of myelin to magnetic susceptibility-

- weighted contrasts in high-field MRI of the brain. *Neuroimage*. 2012;59(4):3967-3975. doi:10.1016/j.neuroimage.2011.10.076
- 3. Brammerloh M, Morawski M, Friedrich I, et al. Measuring the iron content of dopaminergic neurons in substantia nigra with MRI relaxometry. *Neuroimage*. 2021;239:118255. doi:10.1016/j.neuroimage.2021.118255
- 4. Kirilina E, Helbling S, Morawski M, et al. Superficial white matter imaging: Contrast mechanisms and whole-brain in vivo mapping. *Sci Adv.* 2020;6(41). doi:10.1126/sciadv.aaz9281
- Ogawa S, Lee T -M. Magnetic resonance imaging of blood vessels at high fields: In vivo and in vitro measurements and image simulation. *Magn Reson Med.* 1990;16(1):9-18. doi:10.1002/mrm.1910160103
- Ogawa S, Lee T -M, Nayak AS, Glynn P. Oxygenation-sensitive contrast in magnetic resonance image of rodent brain at high magnetic fields. *Magn Reson Med.* 1990;14(1):68-78. doi:10.1002/mrm.1910140108
- Kiselev VG, Posse S. Analytical model of susceptibility-induced MR signal dephasing: Effect
 of diffusion in a microvascular network. *Magn Reson Med.* 1999;41(3):499-509.
 doi:10.1002/(SICI)1522-2594(199903)41:3<499::AID-MRM12>3.0.CO;2-O
- 8. Frøhlich AF, Østergaard L, Kiselev VG. Theory of susceptibility-induced transverse relaxation in the capillary network in the diffusion narrowing regime. *Magn Reson Med.* 2005;53(3):564-573. doi:10.1002/mrm.20394
- 9. Yablonskiy DA, Haacke EM. Theory of NMR signal behavior in magnetically inhomogeneous tissues: The static dephasing regime. *Magn Reson Med.* 1994;32(6):749-763. doi:10.1002/mrm.1910320610
- Lee J, Hirano Y, Fukunaga M, Silva AC, Duyn JH. On the contribution of deoxy-hemoglobin to MRI gray-white matter phase contrast at high field. *Neuroimage*. 2010;49(1):193-198. doi:10.1016/j.neuroimage.2009.07.017
- 11. Sandgaard AD, Kiselev VG, Henriques RN, Shemesh N, Jespersen SN. Incorporating the effect of white matter microstructure in the estimation of magnetic susceptibility in ex vivo mouse brain. *Magn Reson Med.* 2024;91(2):699-715. doi:10.1002/mrm.29867
- Sandgaard AD, Jespersen SN. Predicting Mesoscopic Larmor Frequency Shifts in White Matter With Diffusion MRI—A Monte Carlo Study in Axonal Phantoms. NMR Biomed. 2025;38(3):e70004. doi:10.1002/nbm.70004

- 13. Sandgaard AD, Shemesh N, Østergaard L, Kiselev VG, Jespersen SN. The Larmor frequency shift of a white matter magnetic microstructure model with multiple sources. *NMR Biomed*. 2024;37(8):e5150. doi:10.1002/nbm.5150
- Sandgaard AD, Shemesh N, Kiselev VG, Jespersen SN. Larmor frequency shift from magnetized cylinders with arbitrary orientation distribution. *NMR Biomed*. 2023;36(3):e4859. doi:10.1002/nbm.4859
- 15. Kiselev VG. Larmor frequency in heterogeneous media. *J Magn Reson*. 2019;299:168-175. doi:10.1016/j.jmr.2018.12.008
- Ruh A, Emerich P, Scherer H, Novikov DS, Kiselev VG. Observation of magnetic structural universality using transverse NMR relaxation. Published online October 11, 2018. doi:10.48550/arxiv.1810.04847
- Yablonskiy DA, Sukstanskii AL. Generalized Lorentzian Tensor Approach (GLTA) as a biophysical background for quantitative susceptibility mapping. *Magn Reson Med*. 2015;73(2):757-764. doi:10.1002/mrm.25538
- Wharton S, Bowtell R. Fiber orientation-dependent white matter contrast in gradient echo
 MRI. Proc Natl Acad Sci U S A. 2012;109(45):18559-18564. doi:10.1073/pnas.1211075109
- Sukstanskii AL, Yablonskiy DA. On the role of neuronal magnetic susceptibility and structure symmetry on gradient echo MR signal formation. *Magn Reson Med*. 2014;71(1):345-353. doi:10.1002/mrm.24629
- Kiselev VG, Posse S. Analytical theory of susceptibility induced nmr signal dephasing in a cerebrovascular network. *Phys Rev Lett.* 1998;81(25):5696-5699. doi:10.1103/PhysRevLett.81.5696
- Sukstanskii AL, Yablonskiy DA. Gaussian approximation in the theory of MR signal formation in the presence of structure-specific magnetic field inhomogeneities. Effects of impermeable susceptibility inclusions. *J Magn Reson*. 2004;167(1):56-67. doi:10.1016/j.jmr.2003.11.006
- Sukstanskii AL, Yablonskiy DA. Gaussian approximation in the theory of MR signal formation in the presence of structure-specific magnetic field inhomogeneities. *J Magn Reson*. 2003;163(2):236-247. doi:10.1016/S1090-7807(03)00131-9
- 23. Möller HE, Bossoni L, Connor JR, et al. Iron, Myelin, and the Brain: Neuroimaging Meets Neurobiology. *Trends Neurosci*. 2019;42(6):384-401. doi:10.1016/j.tins.2019.03.009
- 24. Meguro R, Asano Y, Odagiri S, Li C, Shoumura K. Cellular and subcellular localizations of

- nonheme ferric and ferrous iron in the rat brain: A light and electron microscopic study by the perfusion-Perls and -Turnbull methods. *Arch Histol Cytol*. 2008;71(4):205-222. doi:10.1679/aohc.71.205
- 25. Bloembergen N, Purcell EM, Pound R V. Relaxation effects in nuclear magnetic resonance absorption. *Phys Rev.* 1948;73(7):679-712. doi:10.1103/PhysRev.73.679
- Yablonskiy DA, Sukstanskii AL. Quantum magnetization exchange through transient hydrogen bond matrix defines magnetic resonance signal relaxation and anisotropy in central nervous system. *Sci Rep.* 2025;15(1):2025.04.22.650086. doi:10.1038/s41598-025-07808-7
- 27. Yablonskiy DA. Quantitation of intrinsic magnetic susceptibility-related effects in a tissue matrix. Phantom study. *Magn Reson Med.* 1998;39(3):417-428. doi:10.1002/mrm.1910390312
- 28. Wharton S, Bowtell R. Gradient echo based fiber orientation mapping using R2* and frequency difference measurements. *Neuroimage*. 2013;83:1011-1023. doi:10.1016/j.neuroimage.2013.07.054
- Jensen JH, Chandra R. NMR relaxation in tissues with weak magnetic inhomogeneities.
 Magnetic Resonance in Medicine. doi:10.1002/1522-2594(200007)44:1<144::AID-MRM21>3.0.CO;2-O
- 30. Jensen JH, Chandra R. Strong field behavior of the NMR signal from magnetically heterogeneous tissues. *Magn Reson Med.* 2000;43(2):226-236. doi:10.1002/(SICI)1522-2594(200002)43:2<226::AID-MRM9>3.0.CO;2-P
- 31. Jensen JH, Chandra R, Ramani A, et al. Magnetic field correlation imaging. *Magn Reson Med*. 2006;55(6):1350-1361. doi:10.1002/mrm.20907
- 32. Chen J, Gong NJ, Chaim KT, Otaduy MCG, Liu C. Decompose quantitative susceptibility mapping (QSM) to sub-voxel diamagnetic and paramagnetic components based on gradient-echo MRI data. *Neuroimage*. 2021;242:118477. doi:10.1016/j.neuroimage.2021.118477
- Shin HG, Lee J, Yun YH, et al. χ-separation: Magnetic susceptibility source separation toward iron and myelin mapping in the brain. *Neuroimage*. 2021;240:118371. doi:10.1016/j.neuroimage.2021.118371
- 34. Winther S, Lundell H, Rafael-Patiño J, Andersson M, Thiran JP, Dyrby TB. Susceptibility-induced internal gradients reveal axon morphology and cause anisotropic effects in the diffusion-weighted MRI signal. *Sci Rep.* 2024;14(1):1-18. doi:10.1038/s41598-024-79043-5
- 35. Denk C, Torres EH, Mackay A, Rauscher A. The influence of white matter fibre orientation on MR signal phase and decay. *NMR Biomed*. 2011;24(3):246-252. doi:10.1002/nbm.1581

- 36. Lee J, van Gelderen P, Kuo LW, Merkle H, Silva AC, Duyn JH. T2*-based fiber orientation mapping. *Neuroimage*. 2011;57(1):225-234. doi:10.1016/j.neuroimage.2011.04.026
- 37. Bender B, Klose U. The in vivo influence of white matter fiber orientation towards B0 on T2* in the human brain. *NMR Biomed*. 2010;23(9):1071-1076. doi:10.1002/nbm.1534
- 38. Tax CMW, Kleban E, Chamberland M, Baraković M, Rudrapatna U, Jones DK. Measuring compartmental T2-orientational dependence in human brain white matter using a tiltable RF coil and diffusion-T2 correlation MRI. *Neuroimage*. 2021;236. doi:10.1016/j.neuroimage.2021.117967
- 39. Kor D, Birkl C, Ropele S, et al. The role of iron and myelin in orientation dependent R2* of white matter. *NMR Biomed*. 2019;32(7):e4092. doi:10.1002/nbm.4092
- 40. Birkl C, Doucette J, Fan M, Hernández-Torres E, Rauscher A. Myelin water imaging depends on white matter fiber orientation in the human brain. *Magn Reson Med.* 2021;85(4):2221-2231. doi:10.1002/mrm.28543
- 41. Lenz C, Berger C, Bauer M, Scheurer E, Birkl C. Sensitivity of fiber orientation dependent R2* to temperature and post mortem interval. *Magn Reson Med*. 2021;86(5):2703-2715. doi:10.1002/mrm.28874
- 42. Aggarwal M, Kageyama Y, Li X, Van Zijl PC. B0-orientation dependent magnetic susceptibility-induced white matter contrast in the human brainstem at 11.7T. *Magn Reson Med*. 2016;75(6):2455-2463. doi:10.1002/mrm.26208
- 43. Novikov DS, Jensen JH, Helpern JA, Fieremans E. Revealing mesoscopic structural universality with diffusion. *Proc Natl Acad Sci U S A*. 2014;111(14):5088-5093. doi:10.1073/pnas.1316944111
- 44. Mitra PP, Sen PN, Schwartz LM, Le Doussal P. Diffusion propagator as a probe of the structure of porous media. *Phys Rev Lett.* 1992;68(24):3555-3558. doi:10.1103/PhysRevLett.68.3555
- 45. Ruh A, Emerich P, Scherer H, Novikov DS, Kiselev VG. Observation of magnetic structural universality and jamming transition with NMR. *J Magn Reson*. 2023;353:107476. doi:10.1016/j.jmr.2023.107476
- 46. Torquato S. Hyperuniform states of matter. *Phys Rep.* 2018;745:1-95. doi:10.1016/J.PHYSREP.2018.03.001
- 47. Lee HH, Papaioannou A, Kim SL, Novikov DS, Fieremans E. A time-dependent diffusion MRI signature of axon caliber variations and beading. *Commun Biol.* 2020;3(1):1-13.

- 48. Ronen I, Budde M, Ercan E, Annese J, Techawiboonwong A, Webb A. Microstructural organization of axons in the human corpus callosum quantified by diffusion-weighted magnetic resonance spectroscopy of N-acetylaspartate and post-mortem histology. *Brain Struct Funct*. 2014;219(5):1773-1785. doi:10.1007/s00429-013-0600-0
- 49. Andersson M, Kjer HM, Rafael-Patino J, et al. Axon morphology is modulated by the local environment and impacts the noninvasive investigation of its structure–function relationship. *Proc Natl Acad Sci U S A*. 2020;117(52):33649-33659. doi:10.1073/PNAS.2012533117
- 50. Novikov DS, Fieremans E, Jespersen SN, Kiselev VG. Quantifying brain microstructure with diffusion MRI: Theory and parameter estimation. *NMR Biomed*. 2019;32(4):e3998. doi:10.1002/nbm.3998
- Novikov DS, Kiselev VG, Jespersen SN. On modeling. *Magn Reson Med*. 2018;79(6):3172-3193. doi:10.1002/mrm.27101
- 52. Veraart J, Novikov DS, Fieremans E. TE dependent Diffusion Imaging (TEdDI) distinguishes between compartmental T2 relaxation times. *Neuroimage*. 2018;182:360-369. doi:10.1016/j.neuroimage.2017.09.030
- 53. Dell'acqua VP, Tax CMW, Molendowska M, Jones DK, Kleban E, Parker GD. Abstract title: Measuring compartmental T2 and T2* orientation dependence in white matter. In: *ISMRM Workshop on Diffusion MRI: From Research to Clinic.*; 2022.
- 54. Kaden E, Gyori NG, Rudrapatna SU, et al. Microscopic susceptibility anisotropy imaging. *Magn Reson Med.* 2020;84(5):2739-2753. doi:10.1002/mrm.28303
- 55. Kiselev VG, Novikov DS. *Transverse NMR Relaxation in Biological Tissues*. Vol 182.; 2018:149-168. doi:10.1016/j.neuroimage.2018.06.002
- 56. Jensen JH, Helpern JA, Ramani A, Lu H, Kaczynski K. Diffusional kurtosis imaging: The quantification of non-Gaussian water diffusion by means of magnetic resonance imaging. *Magn Reson Med.* 2005;53(6):1432-1440. doi:10.1002/mrm.20508
- 57. Erickson SJ, Prost RW, Timins ME. The "magic angle" effect: Background physics and clinical relevance. *Radiology*. 1993;188(1):23-25. doi:10.1148/radiology.188.1.7685531
- Yablonskiy DA, Sukstanskii AL, Luo J, Wang X. Voxel spread function method for correction of magnetic field inhomogeneity effects in quantitative gradient-echo-based MRI. *Magn Reson Med.* 2013;70(5):1283-1292. doi:10.1002/mrm.24585
- 59. Wharton S, Bowtell R. Effects of white matter microstructure on phase and susceptibility

- maps. Magn Reson Med. 2015;73(3):1258-1269. doi:10.1002/mrm.25189
- 60. Luo J, He X, Yablonskiy DA. Magnetic susceptibility induced white matter MR signal frequency shifts Experimental comparison between Lorentzian sphere and generalized Lorentzian approaches. *Magn Reson Med.* 2014;71(3):1251-1263. doi:10.1002/mrm.24762
- 61. Ruh A, Kiselev VG. Calculation of Larmor precession frequency in magnetically heterogeneous media. *Concepts Magn Reson Part A Bridg Educ Res.* 2018;47A(1):e21472. doi:10.1002/cmr.a.21472
- 62. Jones DK, Horsfield MA, Simmons A. Optimal strategies for measuring diffusion in anisotropic systems by magnetic resonance imaging. *Magn Reson Med.* 1999;42(3):515-525. doi:10.1002/(SICI)1522-2594(199909)42:3<515::AID-MRM14>3.0.CO;2-Q
- 63. Duyn JH, Schenck J. Contributions to magnetic susceptibility of brain tissue. *NMR Biomed*. 2017;30(4):e3546. doi:10.1002/nbm.3546
- 64. Abdollahzadeh A, Belevich I, Jokitalo E, Sierra A, Tohka J. DeepACSON automated segmentation of white matter in 3D electron microscopy. *Commun Biol.* 2021;4(1):1-14. doi:10.1038/s42003-021-01699-w
- 65. Abdollahzadeh A, Belevich I, Jokitalo E, Tohka J, Sierra A. Automated 3D Axonal Morphometry of White Matter. *Sci Rep.* 2019;9(1):1-16. doi:10.1038/s41598-019-42648-2
- 66. Abdollahzadeh A, Coronado-Leija R, Lee HH, Sierra A, Fieremans E, Novikov DS. Scattering approach to diffusion quantifies axonal damage in brain injury. *Nat Commun* 2025 161. 2025;16(1):9808-. doi:10.1038/s41467-025-64793-1
- 67. Jensen JH, Russell Glenn G, Helpern JA. Fiber ball imaging. *Neuroimage*. 2016;124(Pt A):824-833. doi:10.1016/j.neuroimage.2015.09.049
- 68. Fukunaga M, Li TQ, Van Gelderen P, et al. Layer-specific variation of iron content in cerebral cortex as a source of MRI contrast. *Proc Natl Acad Sci U S A*. 2010;107(8):3834-3839. doi:10.1073/pnas.0911177107
- 69. Schenck JF. The role of magnetic susceptibility in magnetic resonance imaging: MRI magnetic compatibility of the first and second kinds. *Med Phys.* 1996;23(6):815-850. doi:10.1118/1.597854
- Yablonskiy DA, Wen J, Kothapalli SVVN, Sukstanskii AL. In vivo evaluation of heme and non-heme iron content and neuronal density in human basal ganglia. *Neuroimage*. 2021;235:118012. doi:10.1016/j.neuroimage.2021.118012
- 71. Barakovic M, Tax CMW, Rudrapatna U, et al. Resolving bundle-specific intra-axonal T2

- values within a voxel using diffusion-relaxation tract-based estimation. *Neuroimage*. 2021;227:117617. doi:10.1016/j.neuroimage.2020.117617
- 72. Sandgaard A, Kiselev V, Shemesh N, Jespersen S. Towards a Standard Model of Diffusion in White Matter with Phase and Relaxation A Monte-Carlo Study. In: 2024 ISMRM & ISMRT Annual Meeting.; 2024:#0589. doi:10.58530/2024/0589

Supplementary Materials

Investigating time- and orientation-dependent transverse relaxation from magnetic susceptibility of white matter microstructure

Anders Dyhr Sandgaard¹, Rafael Neto Henriques², Noam Shemesh², Sune Nørhøj Jespersen^{1,3}

¹Center of Functionally Integrative Neuroscience, Department of Clinical Medicine, Aarhus University,

Denmark

 ${}^2{\rm Champalimaud\ Research,\ Champalimaud\ Centre\ for\ the\ Unknown,\ Lisbon,\ Portugal}$

³Department of Physics and Astronomy, Aarhus University, Denmark

S1 - Larmor frequency variance inside hollow synthetic axons packed with spheres

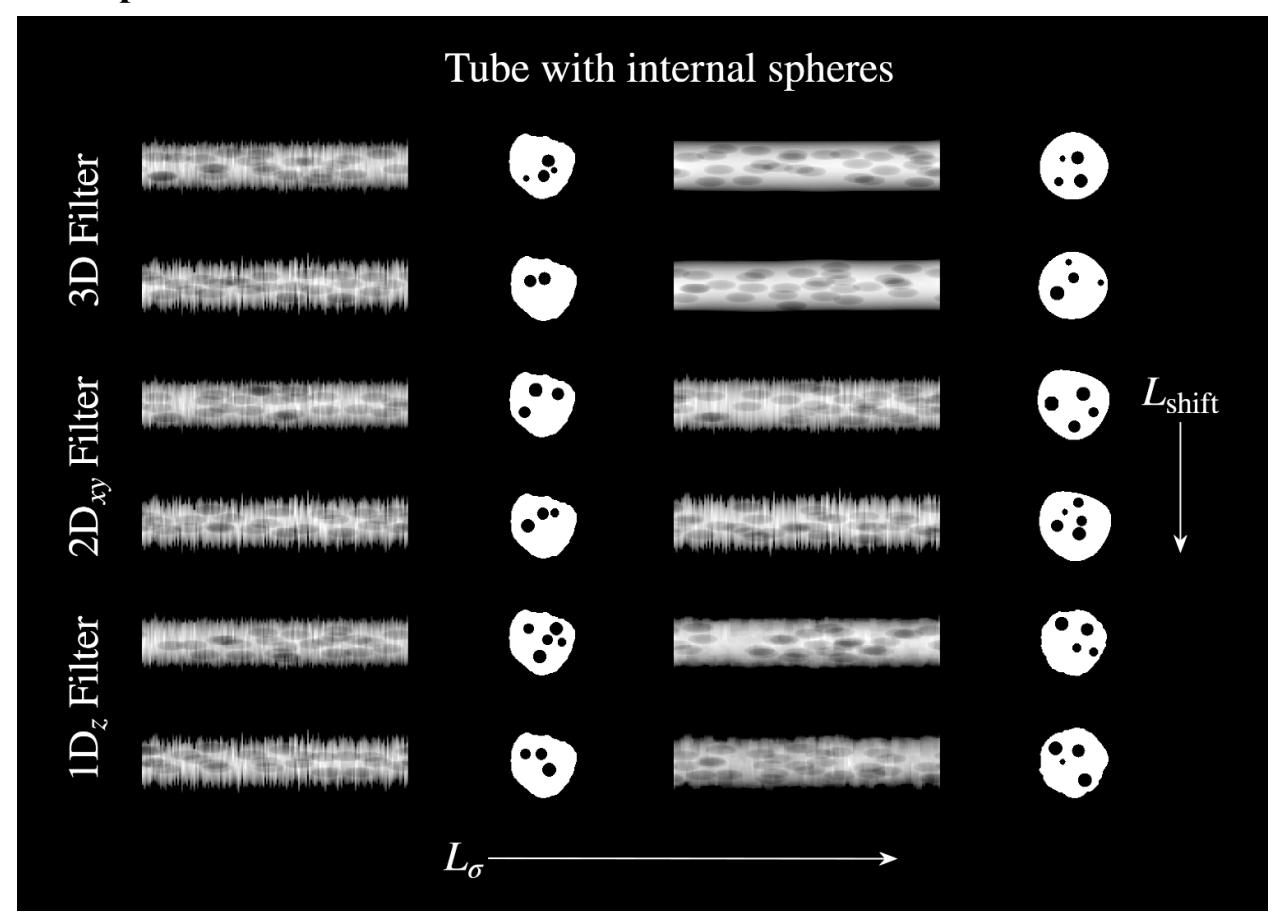


Figure S1 - Overview of synthetic axons filled with randomly packed spheres. A tube with randomly varying radius was generated and each cross-section of the tube was shifted randomly in the radial direction by an amount L_{shift} . First two rows show the tube filtered by a 3D Gaussian filter, where the first two collumns show the tube before smoothing, and the last two rows after smoothing. First row shows without any shift L_{shift} , while the second shows with shift. The second and third rows show axons with 2D Gaussian smoothing perpendicular to the axon, and the latter two rows with 1D smothing longitudinally.

Methods

Figure S1 gives an overview of the synthetic axons considered. First, a cylinder pointing along \hat{z} with length L and radius R_0 , where $L/R_0 = 15$, was discretized on a 3D grid with $L_{grid} = 150 = 7.5R_0 = L/2$ grid points along each dimension. For each cross-sectional layer of the tube, the radius was perturbed according to a normal distribution with zero mean and standard deviation $R_0/4$. The synthetic axon was then hollowed by eroding each cross-sectional layer $R_0/3$ grid points and subtracting it from the original layer. Each layer was then randomly shifted L_{shift} away from its center-of-mass (COM), again picked from a normal distribution

with zero mean, while the standard deviation of the shift was varied across 7 individual simulations ranging from $L_{shift} = 0$ to $R_0/3$. To vary the structural correlation of the synthetic axon's surface morphology, we smoothed the axon by applying either a 1D, 2D or 3D Gaussian filter to the surface, with standard deviation ranging from $L_{\sigma} = 0$ to R_0 across 20 individual simulations. After smoothing, the synthetic axon was again represented by an indicator function $v_{axon}(r)$ (1 inside the layer and otherwise 0) by thresholding. The 2D filter was applied in the *xy*-plane perpendicular to the direction of the axon, while 1D filtering was done along the *z*-axis of the axon.

For each feature combination, we computed the induced Larmor frequency shift $\Omega(\mathbf{r})$ using Eq. Error! Reference source not found. from the synthetic axon sheath described by the indicator function $v_{axon}(\mathbf{r})$. We then computed the magnetic field variance σ^2 inside and outside the synthetic axon j=a,e. $\Omega(\mathbf{r})$ was computed numerically, with zero padding perpendicular to the tube to avoid external fields leaking inside the tube and edge fields on the top and bottom of the synthetic axon. Hence, it is by zero-padding along the axial direction of the synthetic axon that its field appears to come from a tube twice the length of the 3D grid. The magnetizing external field $\mathbf{B}_0 = B_0 \hat{\mathbf{B}}^T$ was oriented along 100 unique orientations $\hat{\mathbf{B}}$ generated using electrostatic repulsion.

We also tested the effect of magnetized spherical inclusions inside the synthetic axon. Here we packed the intra-axonal space with randomly packed spheres all with a radius $R_S = R_0/4$. The density of spheres inside was kept at 10%. As for the tube, we numerically calculated $\Omega(\mathbf{r})$ from the spheres and computed the variance outside the sphere, and inside the synthetic axon, for each measurement direction $\hat{\mathbf{B}}$.

Results

Figure S2 shows the Larmor frequency variance σ^2 inside and outside the synthetic axons, respectively, for the different shifts and filters, while Figure S4 shows the fitting parameters. Here we found Eq. Error! **Reference source not found.** could describe all cases considered.

Figure S3 shows σ^2 caused by the intra-axonal spheres while Figure S4 shows the fitting parameters. Here we see that, for all cases considered here, intra-axonal σ^2 , appears dipolar behaving as $(1 - 3\cos^2(\theta))^2$. Outside the axons, which is isolated from the spheres by the synthetic myelin layer, the variance σ^2 goes as $\sin^4(\theta)$, which is sensible since the field from a cylindrical arrangement of spheres appear as that of a straight cylinder sufficiently far away from its axis. Hence, Eq. **Error! Reference source not found.** can explain the magnetic field variance induced both inside and outside the synthetic axons, and from the spherical sources and myelin-like sheaths.

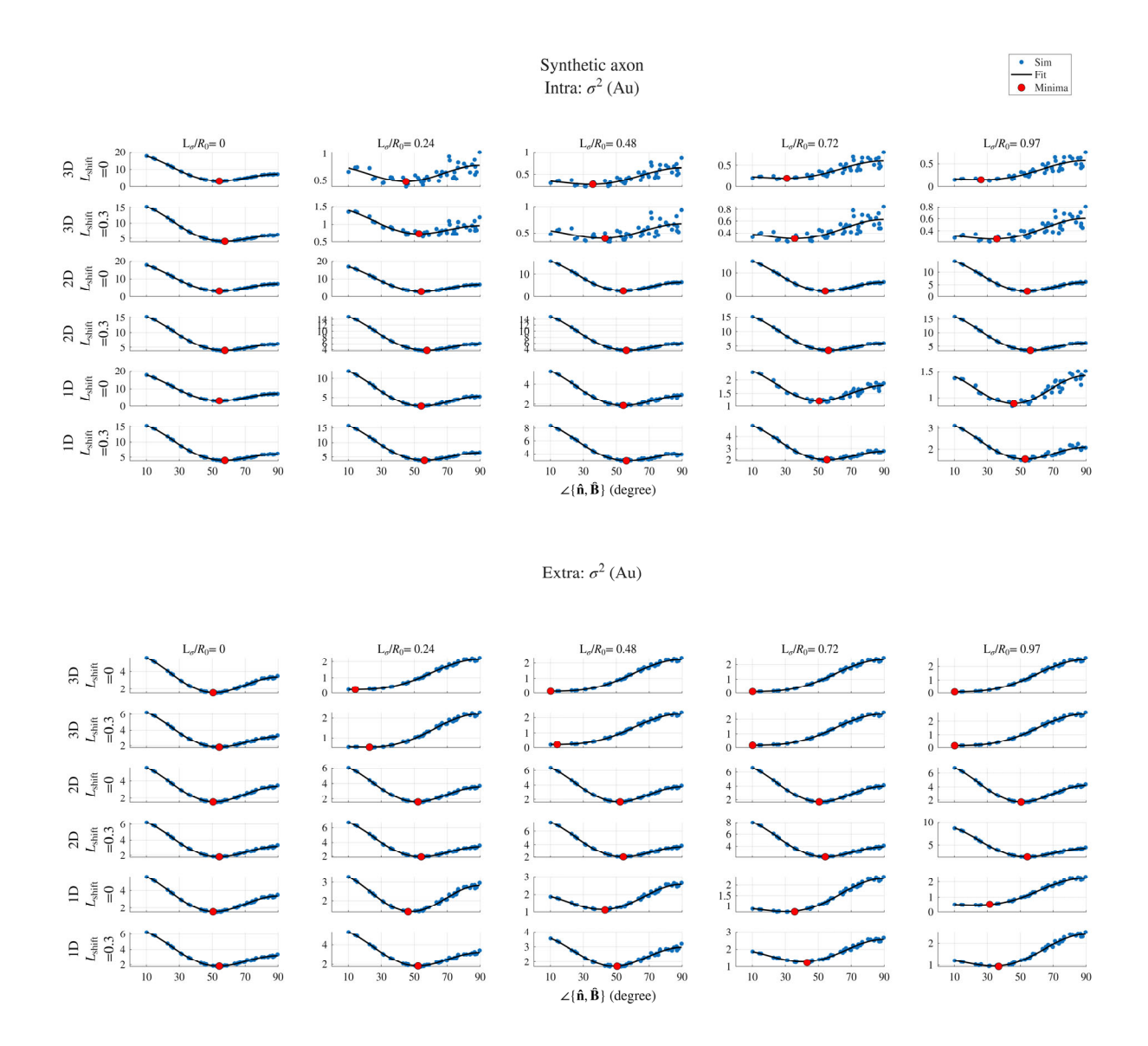


Figure S2 - Larmor frequency variance indeued by synthetic axonal myelin sheath with scalar susceptibility. First six rows show the intra-axonal magnetic field variance for 3D, 2D or 1D Gaussian smoothing and cross-sectional shift L_{shift} . The last six rows show variance outside the synthetic axons. X-axis denotes the angle between B0 and axon.

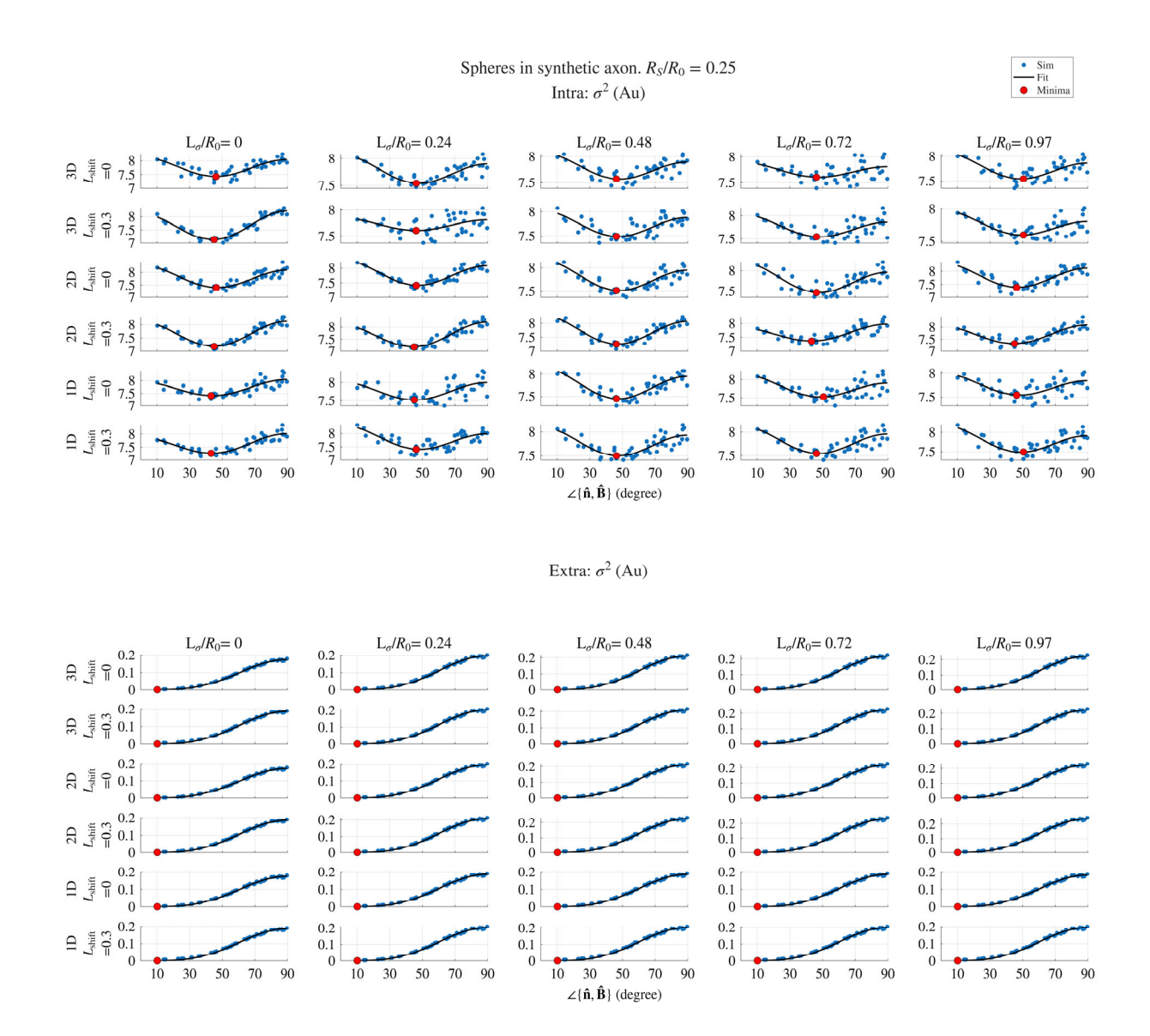
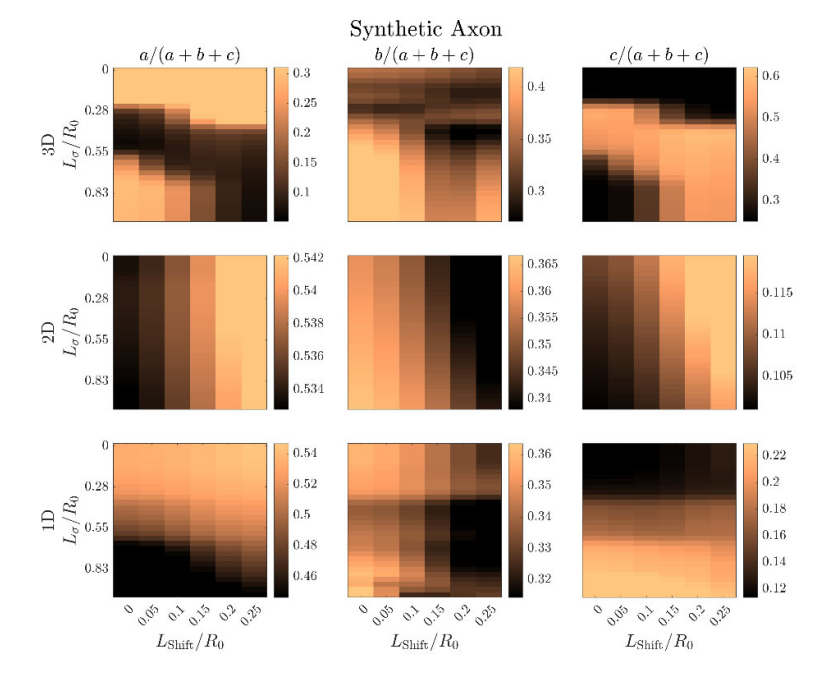
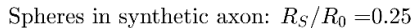


Figure S3 - Larmor frequency variance induced by randomly packed spheres with scalar susceptibility inside a synthetic axon. First six rows show the intra-axonal variance for 3D, 2D or 1D Gaussian smoothing and cross-sectional shift L_{shift} . The last six rows show variance outside the synthetic axons. X-axis denotes the angle between B0 and axon.





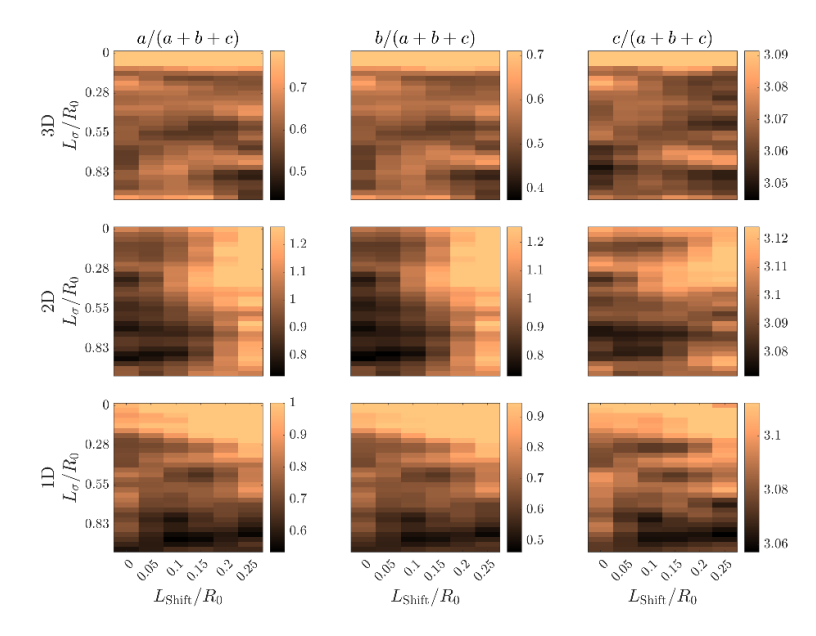


Figure S4 - Parameters of Eq. Error! Reference source not found. after fitting Larmor frequency variance induced inside synthetic axon generated by either the synthetic axons or by randomly packed sphered in the axons. Here is shown for a radius $R_S/R_0=0.25$ for the spheres compared to the mean axon radius. X-axis denoted the amount of cross-section shifts induced for each axon slice, while the y-xais the size of the smoothing filter. First two rows show for 3D Gaussian smoothing, the next two 2D Gaussian smoothing and the latter rows 1D Gaussian smoothing. Colors are clippped in order to visualize the whole range of values.

S2 - Larmor frequency variance inside hollow synthetic axons packed with spheres

We also designed a set of simulations to examine the orientation dependence of Eqs. Error! Reference source not found. and Error! Reference source not found. from a) individual WM axons segmented from electron microscopy (EM), and b) full WM axonal microstructures from EM containing thousands of axons. In both simulations, we considered the individual contribution from Larmor frequency shifts induced i) by the axons and ii) manually introduced intra-axonal spherical inclusions. Every inclusion, also myelin, was assumed to have scalar susceptibility 12,57 in every simulation. We denote the four cases as ai, aii, bi, aii, bi, and bii, respectively.

Methods

a) Larmor frequency variance inside individual realistic axons with varying morphology In the spirit of Winther et al. 35 and Lee et al. 58, we considered the intra-axonal Larmor frequency variance variances $\overline{\sigma^2}$, $\sqrt{(\overline{\sigma^2})^2 - (\sigma^2)^2}$ and $\overline{\Omega^2} - \overline{\Omega}^2$, and extra-axonal variance $\overline{\sigma^2}$ for $B_0 = 7T$ and various orientations $\hat{\mathbf{B}}$. The frequency shift was induced by realistic axons with varying morphological features to assess how these structural variations influence the field variance and whether the resulting orientation dependence can be explained by Eq. Error! Reference source not found.. Error! Reference source not found, provides an overview of the axons analyzed, which were extracted from 8 different white matter substrates segmented from openly available electron microscopy (EM) data (see previous work¹³ for details). Two of the substrates were from tissue affected by traumatic brain injury (TBI). For each substrate, we identified the principal fiber direction and selected a major axon bundle consisting of approximately 2,000 axons aligned predominantly along this direction. As described in our previous study¹³, the axonal microstructure in each substrate was defined by an indicator function v(r) on a 3D grid with resolution of 0.1 um³ (see ref ¹³ for more details). The labels C2-C5 in Error! Reference source not found. are adopted from Winther et al.³⁵, while C6 is an additional case designed to isolate the effect of non-circular cross section. For that, we modified the center of mass for each cross-sectional slice along the main direction of the axon to be equal to remove any slowly varying axial tortuosity, while retaining the original non-circular cross-section. The extra-axonal space outside one axon was here defined by dilating the mask v(r) such that the axon diameter was twice as large and then subtracting v(r). For the myelinated axons in ai, we used an intrinsic scalar susceptibility of $\chi_{\rm m}=-100\frac{\rm ppb}{\zeta_{\rm m}}$ $_{12,57,59}^{12,57,59}$, where ζ_{m} is the volume fraction of axons in the entire microstructure. The local Larmor frequency shift $\Omega(r)$ was calculated numerically 60 using Eq. Error! Reference source not found., with $\chi_m(r) = \chi_m v_m(r)$ for 50 unique orientations of $\hat{\mathbf{B}}$ generated using electrostatic repulsion⁶¹. As our simulation resolution (0.1 μm³) was too coarse to model effects from small

inclusions like ferritin molecules with a radius around 4 nm,⁶² we instead modelled iron-containing cells in *aii*) with a radius of approximately 0.5 µm. We chose a volume fraction of $\zeta_s = 0.05$, and an intrinsic spherical susceptibility of $\chi_s \approx 1100$ ppb, such that the bulk susceptibility in the whole microstructure was $\overline{\chi}_s = \zeta_s \chi_s \approx 55$ ppb. The susceptibility, size and volume fraction could mimic dopaminergic cells containing e.g. ferritin and neuromelanin⁴, and may be found in WM near the Substantia Nigra⁴. Non-overlapping intra-axonal spheres were randomly packed using a previously designed packing generator¹⁵. We assumed the spherical cellular inclusions were impenetrable to water and their water signals fully relaxed, like myelin water. Again, we calculated the local Larmor frequency shift $\Omega(r)$ numerically⁶⁰ using Eq. Error! Reference source not found, with $\chi_s(r) = \chi_s v_s(r)$ for the same 50 orientations of $\hat{\mathbf{B}}$.

b) Larmor frequency variance inside axonal bundle of realistic axons

While the previous simulation considered the self-induced frequency variance from every individual axon only, we next considered $\overline{\sigma^2}$, $\sqrt{(\overline{\sigma^2})^2 - (\overline{\sigma^2})^2}$ and $\overline{\Omega^2} - \overline{\Omega}^2$ in the intra-axonal space, and $\overline{\sigma^2}$ in the extra-axonal space, caused by the entire substrate for all 50 orientations of $\widehat{\bf B}$. This was done bi) for the axonal microstructure, and bii) for intra-axonal spherical inclusions. Hence, the difference between simulation b) compared to a) is that here, induced fields from neighboring axons or spheres are present. To compute the extra-axonal field variance in b), we dilated the intra-axonal mask, similar to simulation a), but now of the ~2000 axons in the bundle. We then multiplied the dilated intra-axonal mask with the negated original masks of myelin and intra-axonal space to segment the extra-axonal space in the vicinity of the axonal bundle. We reused the sphere packing from a), but here we computed the induced field from all the spheres inside the intra-axonal space in the entire microstructure shown in Figure S5.

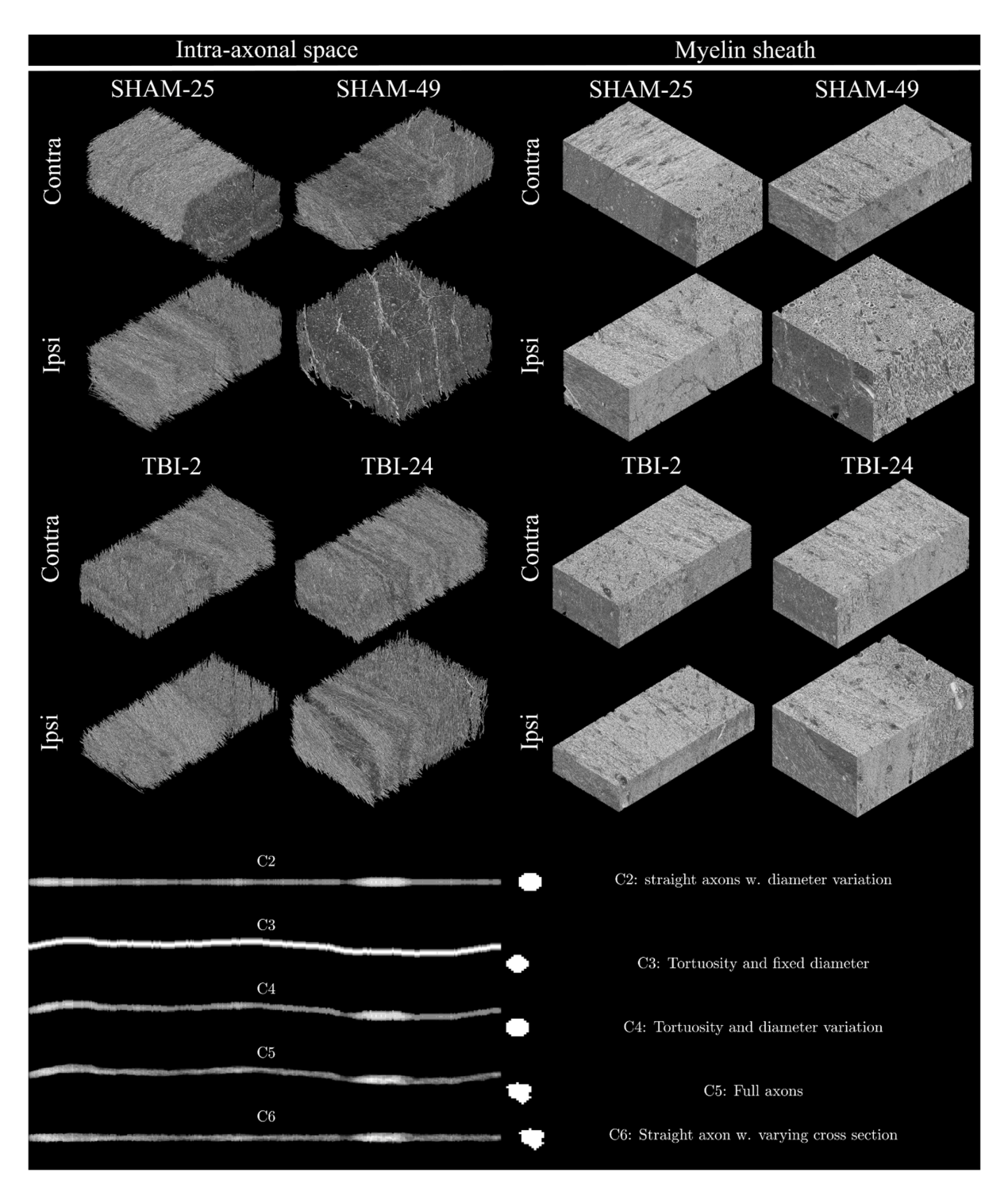


Figure S5 - In-silico white matter axon phantoms used for Monte-Carlo simulations. Eight different substrates from two different SHAM rats labelled 25 and 49 and two different TBI rats labelled 2 and 24 were used for Monte-Carlo simulations. Labels correspond to the original data. For each brain, both ipsilateral (ipsi) and contralateral (contra) tissue samples are considered. The tissue is extracted from the corpus callosum and cingulum bundles. The intra-axonal spaces are used for the Monte-Carlo simulation of diffusing spins, while the myelin sheaths constitute the magnetizable tissue, perturbing the Larmor frequency of the diffusing spins.

For each substrate, we considered the magnetic field variance induced by each axon. In the spirit of Winther et al.35 we

synthesized 6 different axons with varying microstructural features to investigate the intra-axonal and extra-axonal magnetic field average and variance. Labeling was kept as in Winther et al. for consistency.

Results

a) Magnetic field variance inside realistic axons with varying morphology

Figure S6 shows
$$\overline{\sigma^2}$$
, $\sqrt{(\overline{\sigma^2})^2 - (\overline{\sigma^2})^2}$ and $\overline{\Omega^2} - \overline{\Omega}^2$ for realistic axons with varying morphology (C2-C6).

Eq. Error! Reference source not found. consistently captures the orientation dependence across all cases, with parameter values reflecting differences in axonal morphology. Remarkably, none of the simplistic axons are close to the orientation dependence observed in the full axons (C5), which means that all structural features are important when modeling relaxation in axons. Outside the axons, the angular dependence of the magnetic field variance induced by intra-axonal spheres is similar to that of a long cylinder ($\sin^4(\theta) = 1 - 2\cos^2(\theta) + \cos^4(\theta)$).

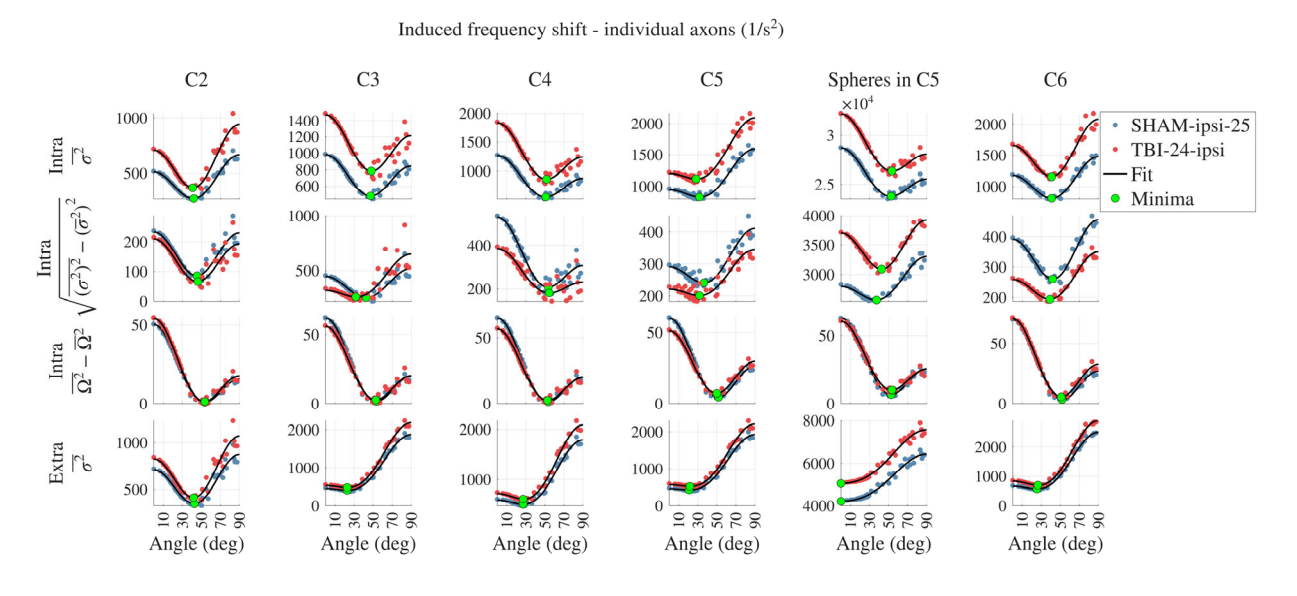


Figure S6—Larmor frequency variance induced by individual axonal myelin sheaths or intra-axonal spherical sources (C5 spheres) versus the angle between B0 and average direction of the axon. First three rows show the variance inside every axon, while the last row shows extra-axonal variance. Labels (C2-C6) indicate the differt morphological features considered (see **Error! Reference source not found.**). Each line shows results for 2 different WM substrates, including fits and minima.

b) Magnetic field variance inside microstructure of realistic axons with varying morphology Figure S7 shows the results for the fields generated by the full microstructure of 2 substrates, in terms of variances within and outside the major fiber bundle. Interestingly, we find upon comparison with Figure S6Error! Reference source not found. that the field variances $\overline{\sigma^2}$, $\sqrt{(\overline{\sigma^2})^2 - (\overline{\sigma^2})^2}$ and $\overline{\Omega^2} - \overline{\Omega}^2$, acquires a

non-negligible contribution from the other magnetized axons. This makes intra-axonal $\overline{\sigma^2}$ more cylinder-like as it behaves as $\sin^4(\theta)$.

The variance $\overline{\sigma^2}$ in Figure S7 caused by intra-axonal spheres from the whole microstructure is comparable in magnitude with the self-induced variance $\overline{\sigma^2}$, as seen in Figure S6Error! Reference source not found. This means that the sphere-induced frequency shift variance largely comes from sources inside the axons. This is also clear upon looking at the extra-axonal variance going as $\sin^4(\theta)$, which is around 5 times weaker in magnitude compared to the variance induced in the intra-axonal space. Equation Error! Reference source not found. could fit all cases well.

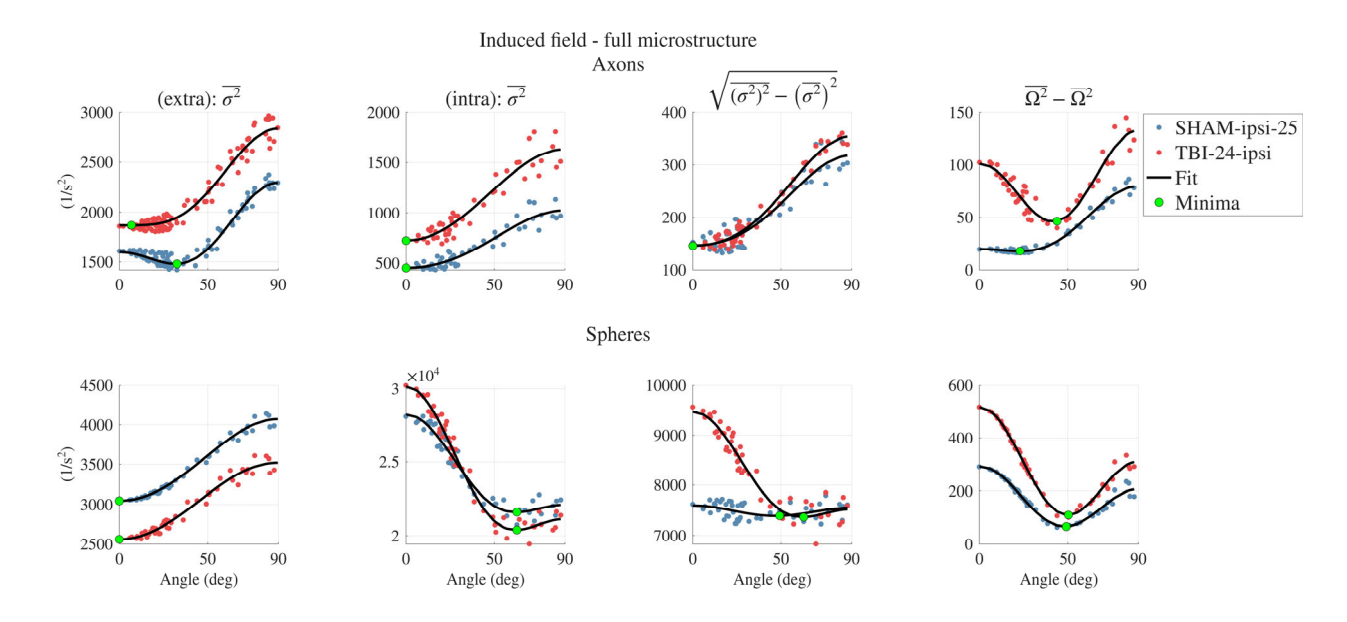


Figure S7 - Larmor frequency variance, induced by axonal myelin sheaths with scalar susceptibility, versus angle between B0 and the average direction of the major fiber bundle. First row shows the intra-axonal variance for 2 different WM substrates, with the first column displays the variance in the extra-axonal space. Second row shows the variance by intra-axonal spherical sources with scalar susceptibility.